Evaluation of emission, performance and combustion characteristics of dual fuelled research diesel engine

Article *in* Environmental Technology · August 2018

DOI: 10.1080/09593330.2018.1509888

4 authors, including:

Senthilkumar Gnanamani
Sathyabama Institute of Science and Technology
53 PUBLICATIONS **245** CITATIONS
SEE PROFILE

Yuvarajan Devarajan
102 PUBLICATIONS **4,144** CITATIONS
SEE PROFILE

Dr Arunkumar T.
CMR Institute of Technology
60 PUBLICATIONS **667** CITATIONS
SEE PROFILE

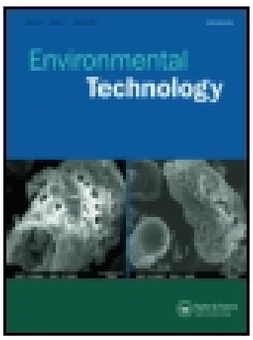

Environmental Technology

ISSN: 0959-3330 (Print) 1479-487X (Online) Journal homepage: http://www.tandfonline.com/loi/tent20

Evaluation of emission, performance and combustion characteristics of dual fuelled research diesel engine

G. Senthilkumar, J.B. Sajin, D. Yuvarajan & T. Arunkumar

To cite this article: G. Senthilkumar, J.B. Sajin, D. Yuvarajan & T. Arunkumar (2018): Evaluation of emission, performance and combustion characteristics of dual fuelled research diesel engine, Environmental Technology, DOI: 10.1080/09593330.2018.1509888

To link to this article: https://doi.org/10.1080/09593330.2018.1509888

Accepted author version posted online: 09 Aug 2018.

Publisher: Taylor & Francis & Informa UK Limited, trading as Taylor & Francis Group

Journal: *Environmental Technology*

DOI: 10.1080/09593330.2018.1509888

Evaluation of emission, performance and combustion characteristics of dual fuelled research diesel engine

Senthilkumar G [1], Sajin JB[2], Yuvarajan D[3,*] Arunkumar T[4]

[1, 4] *Department of Mechanical Engineering, Sathyabama R&D Institute of Science and Technology, Chennai, India.*

[2] *Department of Mechanical Engineering, Sree Buddha College of Engineering, Pattor, Kerala, India.*

[3]*Department of Mechanical Engineering, Vel Tech Rangarajan Dr Sagunthala R&D Institute of Science and Technology, Chennai, India.*

[3,*] *dyuvarajan2@gmail.com*

Abstract:

This study is intended to examine the ignition characteristics of a cashew nut shell biodiesel (C100) along with ethyne (acetylene) as a dual fuel in diesel engine. Cashew nut shell oil is employed in this study owing to non-toxic nature, free from sulphur, biodegradable, and free of aromatics. Ethyne gas was introduced at different flow-rate of 2, 4, 6 litres per minute (lpm). Experimental results revealed that duel fuelling ethyne gas to base fuel (C100) at 6 lpm reduce 18.1% CO, 9.7% HC, 6.87% Smoke with 11.1% increase in NOx emissions. Higher thermal efficiency was observed for ethyne- biodiesel mixture than neat biodiesel in all flow rates. Further, the heat release and peak pressure were enhanced by duel fuelling ethyne gas to base fuel (C100).

Keywords: Performance; Biodiesel; Diesel engine; Emission; Combustion.

1. Introduction

Diesel engines are dominating in transportation, agricultural and power sectors due to their longer reliability higher durability and better fuel economy, under variable conditions compared to petrol engines. However, hazard emissions (NO_x, UHC, PM and smoke) from the diesel engine causes the ozone depletion, greenhouse effect and human health problems [1]. These things have triggered the researchers to a renewable energy source, for the solution to prevent the usage of fossil fuels and hazards environment. At present, the use of biodiesel from vegetable oils in diesel engine has received a much attention by the researchers since it shall be used in existing diesel engines without major change [2]. Further, the favorable bio-fuel properties such as high cetane number and more oxygen by weight have promoted the biodiesel as a promising alternative fuel [3] .The oxygen content in the biodiesel resulted in fewer emissions (HC, CO and smoke) compared to diesel. However, the major problem associated with biodiesel is a high magnitude of NO_x emission and lower efficiency at all engine conditions compared to diesel [4]. Many gaseous fuels are employed in a diesel engine as a dual fuelling to improve the drawbacks of liquid fuels. In this practice, the liquid fuel is supplied to the engine in a traditional manner, while the fuel (gaseous) is mixed evenly with air.

Many studies has experimented dual fuelling in diesel engine and found reduction in all emission [4-6, 22-27]. Mohsin et al. [7] investigated the effect of biodiesel (cooking oil waste) on diesel engine fuelled with diesel and Compressed Natural Gas (CNG) combinations. Biodiesel (Cooking oil) was fuelled at 5, 10, 15 and 20% to the diesel duel fuel. They found a drop in NO_X emissions for biodiesel than by fuelling CNG. However, NO_X emissions were lower than the neat biodiesel operation. They found a higher measure of HC emissions for biodiesel operation when compared to neat diesel at all blends. In addition, they also concluded that an increase in engine power when fuelled with biodiesel and CNG combinations at higher speed. Ethyne gas is obtained from limestone, coal and water. The properties of ethyne are similar to hydrogen gas. An abundance studies have been conducted by using ethyne as dual fuel with diesel and biodiesel and reported the positive combustion and emission characteristics [8-10, 21]

Choudhary et al. [8], Basha and Rao [9], Srivastava et al. [10] employed ethyne in a stationary diesel engine. They found a significant drop in all the emissions by making use of ethyne as an additional fuel. However, NO_X emissions were found to increase by dual fuelling ethylene. This work paves a way on exploring the technological feasibility of employing C100 in a diesel

engine. It has high flash and boiling point, low energy density (Volumetric) and vapor pressure and better lubricating property [3, 12]. India roughly produces 520,000 tons/ year and ranks first for cashew production) [13, 14]. This study is aimed to examine the ignition characteristics of a neat cashew nut shell biodiesel (C100) along with ethyne (acetylene) as a dual fuel in diesel engine.

2. Materials and reagents

2.1. **Biodiesel**

Biodiesel is produced from raw oil through the transesterification method [31, 32]. This method utilizes potassium hydroxide (catalyst) and methanol (alcohol). The raw oil is preheated to 65° C and mixed to a solution containing alcohol and catalyst. The standard molar ratio of oil and alcohol is 6:1. The resultant mixture is heated above 75ºC where the entire methanol present in the mixture gets evaporated for separation of ester and glycerol. The detailed list of properties of C100 and diesel is listed in Table 1.

Table 1. Properties of Tested fuels

PROPERTIES	C100	Diesel	METHOD
Water (%)	0.09	0.004	ASTM D2709
Density @ 18^{O}C (gm/cc)	0.882	0.82	ASTM D4052
Kinematic Viscosity at 35°C	3.85	2.5	ASTM D445
Calorific Value (kJ/kg)	38010	42950	ASTM D240
Cetane Number (CN)	54	46	ASTM D976
Flash point (^{O}C)	140	50	ASTM D93
Cloud point (^{O}C)	10	-17	ASTM D2500
Pour point (^{O}C)	7.9	-30	ASTM D97
C (%)	79	-	ASTM D5291
H(%)	9	-	ASTM D5291
O(%)	12	-	-

2.2. **Experimental setup**

A 5.2 kW naturally aspirated DI diesel engine is utilized for the experimentation. Figure 1 shows the schematic of the engine set up and engine specification is shown in Table 3. The test engine is connected to a dynamometer (eddy current type) for applying loads. The exhaust gases, such as CO, CO_2, NOx, and HC are quantified by using AVL Digas 444 five-gas analyzer [34]. Ethyne gas generator is employed to produce ethyne gas from water and calcium carbide at an atmospheric pressure. The detailed list of uncertainty percentage of various parameters is listed in Table 4.

2.3 Safety Measures taken during the experimentation

The cylinder containing ethyne is held in an upright position. All the necessary actions were taken to avoid leakage of gas during experimentation. A pressure-reducing regulator is employed for varying the flow rate of ethyne from the cylinder. The pressure of the cylinder is maintained below 15 psi to ensure safety. Approved hoses and fittings were employed during experimentation. In addition, soapy water was kept ready to identify any leakage in the cylinder containing ethyne. Cylinder valve is cracked instantly to blow the dirt out of the nozzles before attaching the pressure regulator. Table 3 shows the chemical properties of ethyne.

Figure. 1 Photographic of Engine test bench

Table 2. Ethyne Properties

PROPERTIES	ETHYNE
Density (kg/m3)	1.06
Self-ignition temperature	596 (K)
Adiabatic flame temperature	2,500 (K)
Calorific value	51,121 (kJ/m3)
Speed of Deflagration	2.31(m/s)
Energy during Ignition	20 (kJ/ kg)
Calorific value	3,314 (kJ/kg)

Table 3. Specification of Experimental Setup

Type	Apex Innovation 240PE
Rated Power	5.2 kW
Speed	1600 rpm
Diameter	87.5 mm
Length	110mm
Cooling	Water
Injection style	Pump-line-nozzle
Number of holes	3
Injection timing	21^0 bTDC

Table 4. List of uncertainty percentage of various parameters

Measured Quantity	**Range**	**Uncertainties**
CO	0-5000 ppm	±0.5 (%)
HC	0-20000	±0.1 (%)
NOx	0-5000 ppm	±0.3 (%)
Smoke	AVL 437	±1.1 (%)

3. Results and discussion

3.1. **Hydrocarbons [HC]**

HC emission for C100, C100 and ethyne (2 lpm), C100 and ethyne (4 lpm), C100 and ethyne (6 lpm) and Diesel is revealed in Figure 2. HC emission from C100 is inferior than diesel on account of its percentage of oxygen that leads to improved and complete combustion [3, 15]. HC emissions reduce with a load. Increase in load rises the temperature and lower the HC emissions as in the case of CO emission [16]. HC emissions from C100, ethyne (2 lpm), C100, ethyne (4 lpm), C100, and ethyne (6 lpm) is lower than C100. Ethyne exhibits higher flame velocity, which aids the improved combustion and lower HC emissions [17, 21]. Further, ethyne present in biodiesel exhibit superior flame-speed and improve the combustion process thereby lowering HC emissions. HC emission is found to be higher for C100 and ethyne (2 lpm) followed by for C100 and ethyne (4 lpm) and for C100 and ethyne (6 lpm). This result matches with different literatures [8-11, 17, 21] that reported similar HC variation of diesel engine

powered by different liquid and gaseous fuel mixture. Overall HC emissions for C100, C100 and ethyne (2 lpm), C100 and ethyne (4 lpm), C100 and ethyne (6 lpm) and Diesel is 257, 229, 209, 173 and 284 ppm respectively at all load conditions.

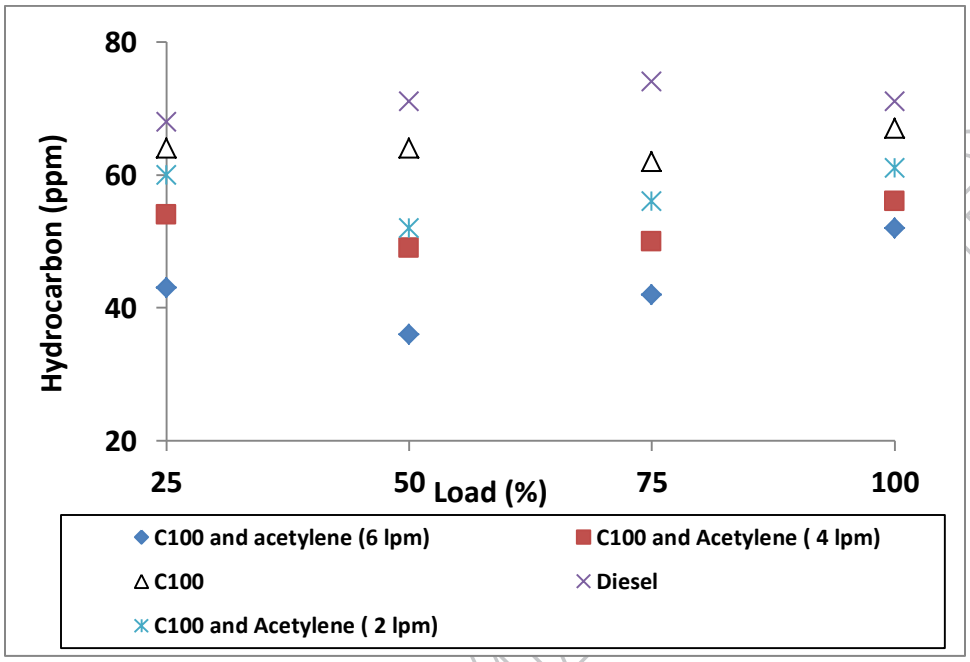

Figure 2. Variation of hydrocarbon emissions across the engine loads

3.2 Carbon monoxide [CO]

CO emission for C100, C100 and ethyne (2 lpm), C100 and ethyne (4 lpm), C100 and ethyne (6 lpm) and Diesel is revealed in Figure 3. CO emission from biodiesel is lower than diesel at all loads. Biodiesel contains a higher percentage of oxygen than diesel, which leads to improved and complete combustion [3, 15]. CO emissions reduce with a load for all the test fuels. Increase in load rises the temperature; augment the combustion rate and lower the CO emissions [16]. CO emissions from C100, ethyne (2 lpm), C100, ethyne (4 lpm), C100, and ethyne (6 lpm) is lower than C100. Dual fuelling ethyne at different rates increases the flammability of the mixture and lower CO emissions [17, 18, 21]. In addition, ethyne enhance the combustion process, lowers CO emission because of its extra energy content, and flame velocity, and extensive ignition limit [34]. CO emission is found to be higher for C100 and ethyne (2 lpm) followed by for C100 and ethyne (4 lpm) and for C100 and ethyne (6 lpm). This result matches with different literatures [8-11, 17, 21] that reported similar CO variation of diesel

engine powered by different liquid and gaseous fuel mixture. Overall CO emission for C100, C100 and ethyne (2 lpm), C100 and ethyne (4 lpm), C100 and ethyne (6 lpm) and Diesel is 0.27, 0.22, 0.16, 0.12 and 0.32 % respectively at all load conditions.

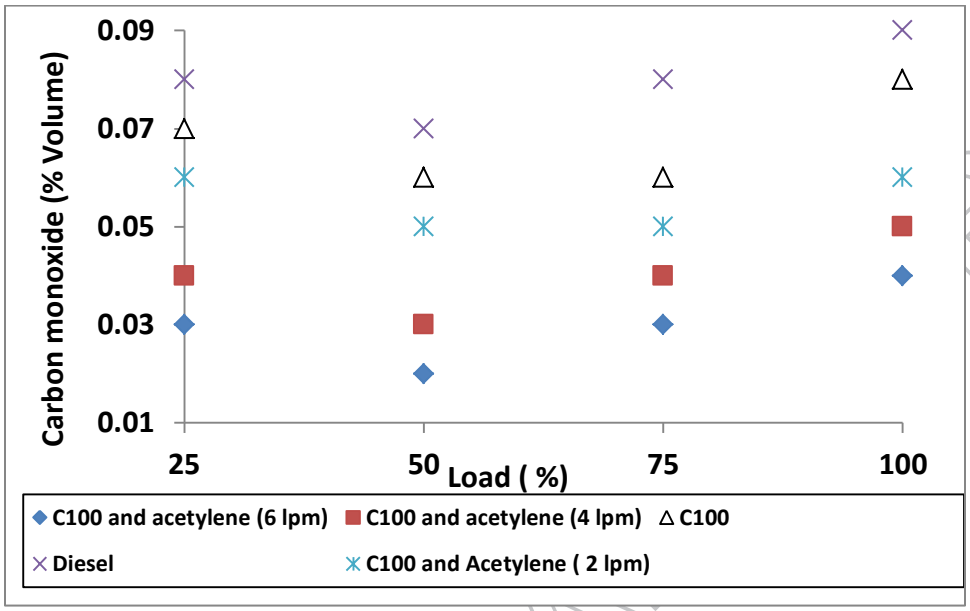

Figure 2. Variation of Carbon monoxide emissions across the engine loads

3.3. **Oxides of nitrogen [NO_x]**

NO_X emission for C100, C100 and ethyne (2 lpm), C100 and ethyne (4 lpm), C100 and ethyne (6 lpm) and Diesel is revealed in Figure 4. With rise in load, the NO_X emission is increased. This is caused by high in-cylinder temperature with increase in load [3]. NO_X emission from C100 is higher than diesel. The O_2 present in C100 leads to higher gas temperature and higher NO_X [15]. During ethyne dual fuelling, NO_X emission increases at all load. The improvement in calorific value of ethyne-biodiesel leads to improved gas temperature originating NO_X emissions [8, 9]. NO_X emission is found to be higher for C100 and ethyne (6 lpm) followed by for C100 and ethyne (4 lpm) and for C100 and ethyne (2 lpm). This result matches with different literatures [8-11, 17, 21] that reported similar NO_X variation of diesel engine powered by different liquid and gaseous fuel mixture. Overall NO_X emission for C100, C100 and ethyne (2 lpm), C100 and ethyne (4 lpm), C100 and ethyne (6 lpm) and Diesel is 3683, 4064, 4352, 4775 and 3112 ppm respectively at all load conditions.

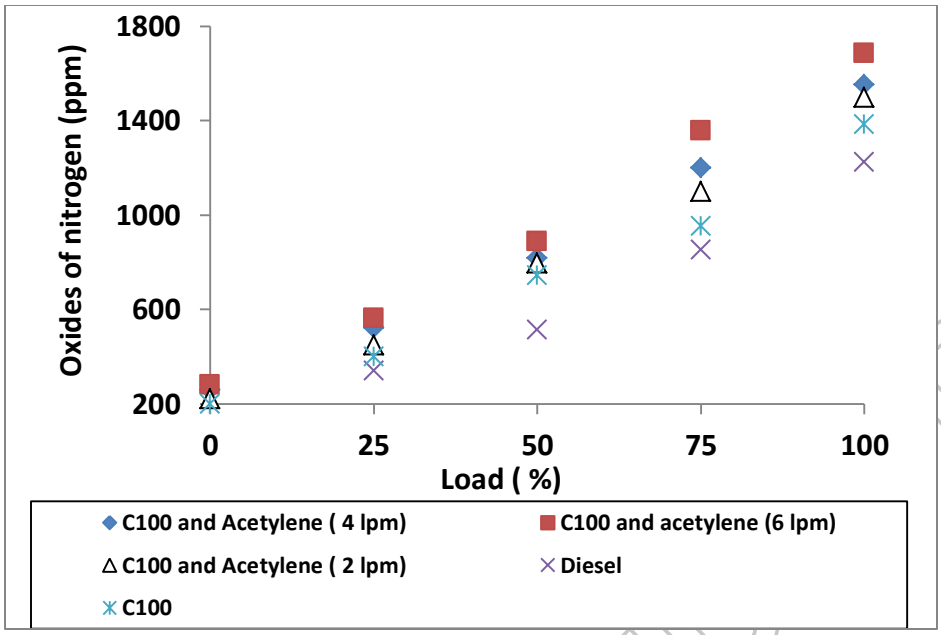

Figure 4.Variation of oxides of nitrogen emissions across the engine load

3.4. **Smoke opacity**

Smoke emission for C100, Diesel, C100 and ethyne (2 lpm), C100 and ethyne (4 lpm), C100 and ethyne (6 lpm) is revealed in Figure 5. With rise in load, the pressure and temperature is increased which in turn enhance the combustion and lower smoke [19]. Smoke emission from C100 is lower compared to diesel. Enhanced oxygen in C100 promotes complete combustion and significantly reduces the smoke opacity [3, 15]. Smoke emissions from C100, ethyne (2 lpm), C100, ethyne (4 lpm), C100, and ethyne (6 lpm) is lower than C100. Dual fuelling ethyne at different rates increases the flammability of the mixture and lower CO emissions. The enhanced heat transfer rate and better air-fuel mixing decrease the Smoke emission of ethyne- biodiesel mode [8, 10, 21]. Smoke emission is found to be higher for C100 and ethyne (2 lpm) followed by for C100 and ethyne (4 lpm) and for C100 and ethyne (6 lpm). This result matches with different literatures [8-11, 17, 21] that reported similar smoke variation of diesel engine powered by different liquid and gaseous fuel mixture. Overall Smoke opacity (%) for C100, C100 and ethyne (2 lpm), C100 and ethyne (4 lpm), C100 and ethyne (6 lpm) and Diesel is 45.5, 42.8, 37.7, 32.3 and 49.5 ppm respectively at all load conditions.

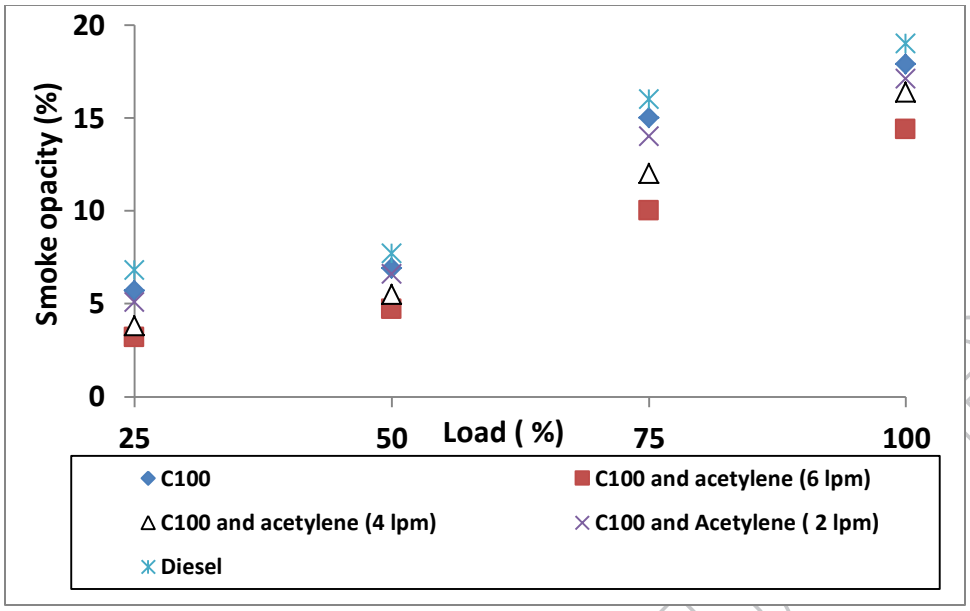

Figure 5. Variation of smoke emissions across the engine load

3.5. **Carbon dioxide [CO_2]**

Carbon dioxide emission for C100, C100 and ethyne (2 lpm), C100 and ethyne (4 lpm), C100 and ethyne (6 lpm) and Diesel is revealed in Figure 6. With the increase in load, the pressure and temperature is increased and resulting in higher CO_2 emission [15]. Biodiesel emits higher CO_2 emission than from diesel owing to natural O_2 existing in C100 [19]. CO_2 emissions from C100, ethyne (2 lpm), C100, ethyne (4 lpm), C100, and ethyne (6 lpm) is higher than C100. The better air-fuel mixing and enhanced heat transfer rate of ethyne-C100 increases the CO_2 emission [10, 21, 36]. Further, the introduction of ethyne to biodiesel produces a homogeneous mixture of fuel and lowers the CO_2 emission [16, 17, 21]. CO_2 emission is found to be higher for C100 and ethyne (6 lpm) followed by for C100 and ethyne (4 lpm) and for C100 and ethyne (2 lpm). This result matches with different literatures [8-11, 17, 21, 24] that reported similar CO_2 variation of diesel engine powered by different liquid and gaseous fuel mixture. Overall CO_2 emission for C100, C100 and ethyne (2 lpm), C100 and ethyne (4 lpm), C100 and ethyne (6 lpm) and Diesel is 24.3, 25.9, 27.3, 29.2 and 22.4 % volume respectively at all load condition.

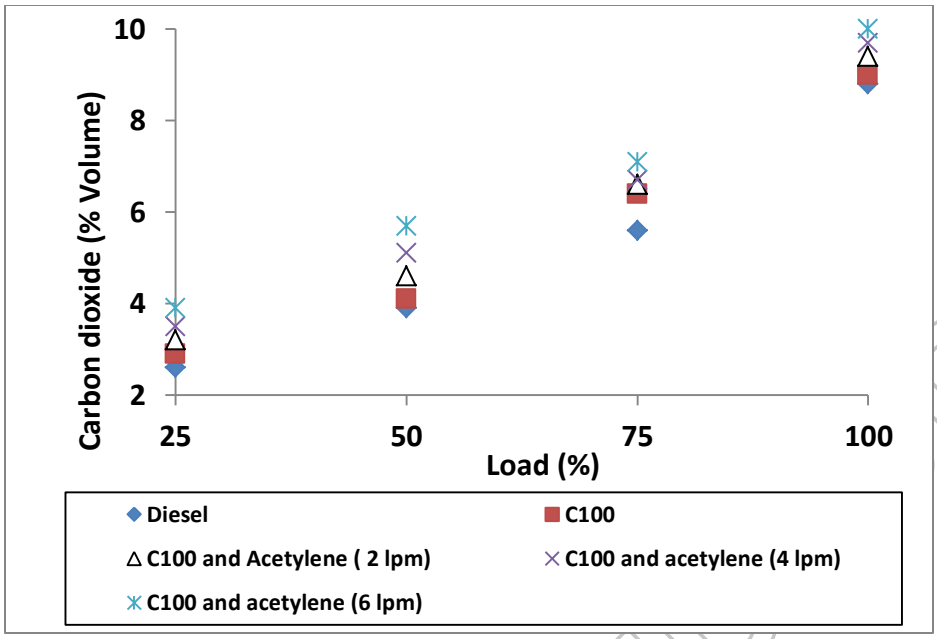

Figure 6. Variation of carbon dioxide emissions across the engine load

3.6 Brake thermal efficiency [BTE]

BTE of C100, C100 and ethyne (2 lpm), C100 and ethyne (4 lpm), C100 and ethyne (6 lpm) and diesel is revealed in Figure 7. BTE increases with a load for all the fuel. Combustion temperature increases with load and aids the combustion process and increase BTE [3]. BTE is higher in ethyne-C100 (2, 4 and 6 lpm) than C100. Ethyne offers a better flame velocity leading to an improved rate of combustion and higher BTE [9, 10, 21]. BTE is found to be higher for C100 and ethyne (6 lpm) followed by for C100 and ethyne (4 lpm) and for C100 and ethyne (2 lpm). This result matches with different literatures [8-11, 17, 21, 24] that reported similar BTE variation of diesel engine powered by different liquid and gaseous fuel mixture. BTE for C100, C100 and ethyne (2 lpm), C100 and ethyne (4 lpm), C100 and ethyne (6 lpm) and Diesel is 23.4, 27.6, 28.1, 28.6, and 29.3 % respectively at full load condition.

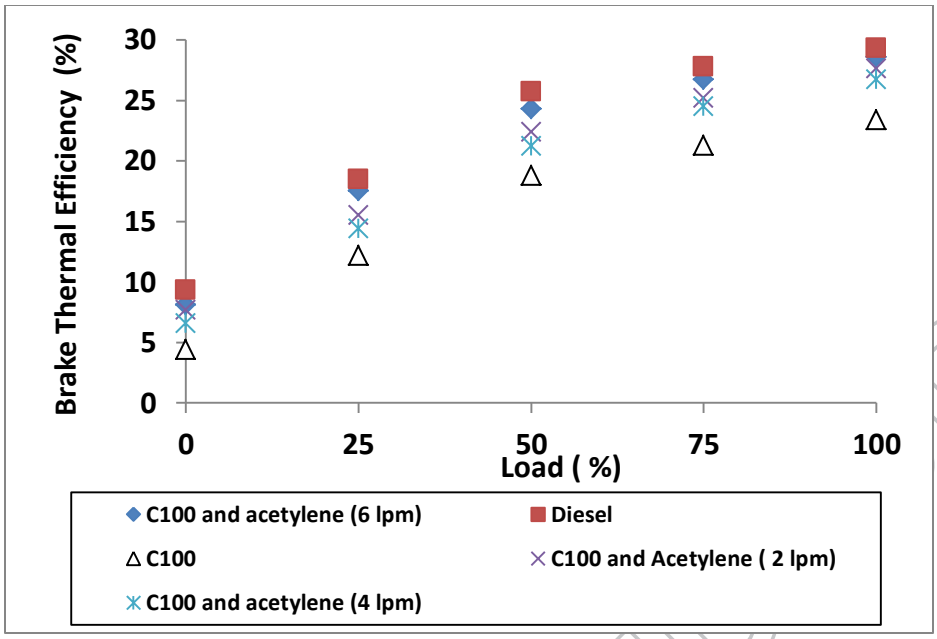

Figure 7. Variation of Brake thermal efficiency across the engine load

3.7 Pressure Rise

The pressure rise of C100, C100 and ethyne (2 lpm), C100 and ethyne (4 lpm), C100 and ethyne (6 lpm) and diesel is revealed in **Figure 8**. The peak pressure value of C100 is 43.14 bar, whereas the diesel exhibits 40.23 bar. The increase in the peak pressure value of C100 is due to longer delay-period associated with oxygenated C100 [11, 18, 27, 28]. It is observed that by dual fuelling 2, 4 and 6 lpm of ethyne to C100 observe a considerable increase in Peak pressure. Faster energy release and high diffusion rate of ethyne attributable to the higher flame velocity of propagation after ignition and higher peak pressure [19, 20]. Peak pressure is found to be higher for C100 and ethyne (6 lpm) followed by for C100 and ethyne (4 lpm) and for C100 and ethyne (2 lpm). This result matches with different literatures [8-11, 17, 21, 24] that found similar observation of engine powered by different liquid and gaseous fuel mixture.

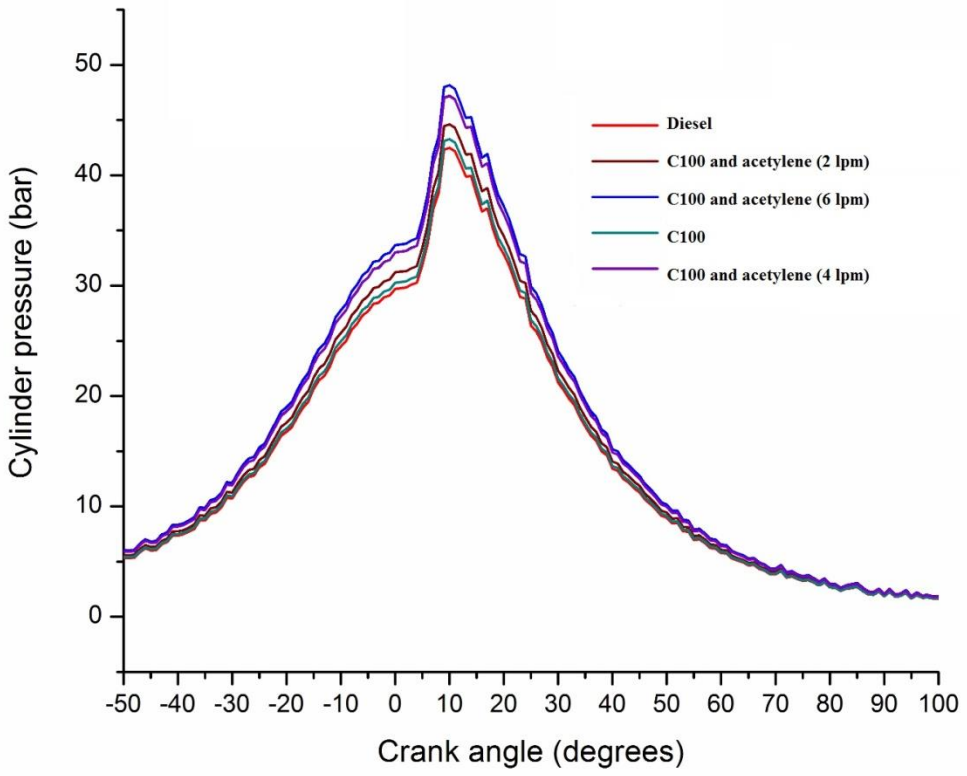

Figure 8.Variation of peak pressure with crank angle at 100% load

3.8 Heat Release Rate

The HRR of C100, C100 and ethyne (2 lpm), C100 and ethyne (4 lpm), C100 and ethyne (6 lpm) and diesel is revealed in **Figure 9.** The experimental result of test fuels indicates that the maximum HRR value of C100 is lower than diesel. The maximum HRR for diesel and C100 are 49.12 and 36.45 J/degCA**.** This may be due to longer delay-period of C100, which can increase the fuel accumulation before the starting of ignition. Further, Diesel has high heating value and produces higher HRR [21]. It is observed that by dual fuelling 2, 4 and 6 lpm of ethyne to C100 observe a rise in HRR. Faster energy release and high diffusion rate of ethyne attributable to the higher flame velocity of propagation after ignition increases HRR [19, 20]. This result matches with different literatures [18-21] that reported similar heat release variation of diesel engine powered by different liquid and gaseous fuel mixture.

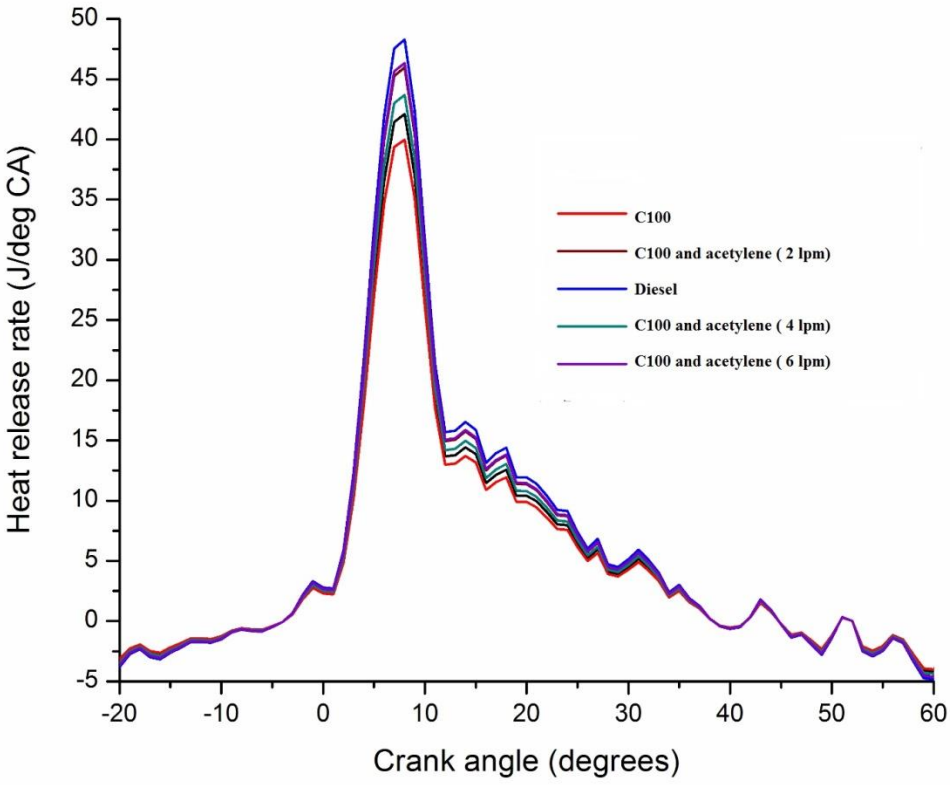

Figure 8.Change in HRR with crank angle at 100% load

Conclusion

A research CI engine was fueled with C100, diesel, and by dual fuelling ethyne gas to base fuel (C100) at 2, 4, and 6 lpm. Ignition characteristics of the test fuels have been studied and analyzed by comparing with the neat baseline diesel. The primary findings of this experimental study is recapitulated below

- CO emission of diesel is highest among all fuels. However, upon on comparison with different fuels, C100 and ethyne (6 lpm) has a lowest compared to other fuel probably owing to high diffusion rate. CO emission is reduced by 9.25%, 16.64% and 18.1% respectively for C100, ethyne (2 lpm), C100, ethyne (4 lpm), C100, and ethyne (6 lpm) when compared to C100.
- HC emission are reduced by 5.44%, 8.14% and 9.72% respectively for C100 and ethyne (2 lpm), C100 and ethyne (4 lpm) and C100 and ethyne (6 lpm) when compared to C100

respectively owing to low carbon combustion activation temperature **and improved hydrocarbon oxidatio**n of ethyne

- NO_X emission is increased for C100 when compared to diesel. However, upon on comparison with different fuels, C100 and ethyne (6 lpm) has a highest compared to other fuel probably owing to higher flame velocity of propagation after ignition of ethyne. NO_X emission is increased by 2.21 %, 3.36% and 4.11% respectively for C100 and ethyne (2 lpm), C100 and ethyne (4 lpm) and C100 and ethyne (6 lpm) when compared to C100.
- Smoke emission are reduced by 3.46%, 5.05% and 6.87% respectively for C100 and ethyne (2 lpm), C100 and ethyne (4 lpm) and C100 and ethyne (6 lpm) when compared to C100 respectively owing to low carbon combustion activation temperature and improved hydrocarbon oxidation of ethyne.
- CO_2 emission of C100 is highest than diesel. However, upon on comparison with different fuels, C100 and ethyne (6 lpm) has a highest compared to other fuel probably owing to higher flammability of ethyne. CO_2 emission is increased by 3.21%, 3.86% and 4.42% respectively for C100, ethyne (2 lpm), C100, ethyne (4 lpm), C100, and ethyne (6 lpm) when compared to C100.
- BTE of C100 is least comparing other fuels. C100 when subjected to addition of ethyne has a significant improvement in BTE. BTE is improved by 2.1%, 2.8% and 3.01% respectively for C100, ethyne (2 lpm), C100, ethyne (4 lpm), C100, and ethyne (6 lpm) respectively when compared to C100 owing to its higher flammability.
- Peak pressure and HRR is higher for C100 than diesel. Further, Peak pressure and HRR is further increased for C100, ethyne (2 lpm), C100, ethyne (4 lpm), C100, and ethyne (6 lpm) respectively when compared to C100 owing to its higher flammability and higher flame velocity of propagation of ethyne.

REFERENCES

[1] Anderson A, Devarajan Y, Nagappan B. Effect of injection parameters on the reduction of NOx emission in neat bio-diesel fuelled diesel engine. Energy Sources, Part A: Recovery, Utilization, and Environmental Effects. 2017;40(2):186–92.

[2] Joy N, Devarajan Y, Nagappan B, Anderson A. Exhaust emission study on neat biodiesel and alcohol blends fueled diesel engine. Energy Sources, Part A: Recovery, Utilization, and Environmental Effects . 2017; 40(1):115–9.

[3] Devarajan Y, Nagappan BK, Munuswamy DB. Performance and emissions analysis on diesel engine fuelled with cashew nut shell biodiesel and pentanol blends. Korean Journal of Chemical Engineering . 2017; 34(4):1021–6.

[4] Yousefi A, Birouk M, Guo H. An experimental and numerical study of the effect of diesel injection timing on natural gas/diesel dual-fuel combustion at low load. Fuel. 2017; 203:642–57.

[5] Yousefi A, Guo H, Birouk M. An experimental and numerical study on diesel injection split of a natural gas/diesel dual-fuel engine at a low engine load. Fuel. 2018; 212:332–46. Available from: http://dx.doi.org/10.1016/j.fuel.2017.10.053

[6] Tarabet L, Loubar K, Lounici MS, Khiari K, Belmrabet T, Tazerout M. Experimental investigation of DI diesel engine operating with eucalyptus biodiesel/natural gas under dual fuel mode. Fuel. 2014; 133:129–38.

[7] R. Mohsin, Z. A. Majid, A. H. Shihnan, N. S. Nasri, Z. Sharer. Effect of Biodiesel Blend on Exhaust Emission and Engine Performance of Diesel Dual Fuel Engine. Iranica Journal OF Energy & Environment. 2015; 6(3).

[8] Choudhary KD, Nayyar A, Dasgupta MS. Effect of compression ratio on combustion and emission characteristics of C.I. Engine operated with ethyne in conjunction with diesel fuel. Fuel. 2018; 214:489–96.

[9] Khader Basha S, Rao PS. Experimental Investigation of Performance of Ethyne Fuel Based Diesel Engine. International Journal of Advancements in Technology [Internet]. OMICS Publishing Group; 2015;07(01). Available from: http://dx.doi.org/10.4172/0976-4860.1000151

[10] Srivastava AK, Soni SL, Sharma D, Jain NL. Effect of injection pressure on performance, emission, and combustion characteristics of diesel–ethyne-fuelled single cylinder stationary CI engine. Environmental Science and Pollution Research. 2017 Available from: http://dx.doi.org/10.1007/s11356-017-1070-3

[11] Srivastava AK, Soni SL, Sharma D, Sonar D, Jain NL. Effect of compression ratio on performance, emission and combustion characteristics of diesel–ethyne-fuelled single-cylinder stationary CI engine. Clean Technologies and Environmental Policy. 2017; 19(5):1361–72.

[12] Devarajan Y, Jayabal R kumar, Ragupathy D, Venu H. Emissions analysis on second generation biodiesel. Frontiers of Environmental Science & Engineering. 2016; 24; 11(1).

[13] Akinhanmi T F, Atasie V N, Akintokun P O. Chemical composition and physicochemical properties of cashew nut (Anacardium occidentale) oil and cashew nut shell liquid. Journal of Agriculture, Food and Environmental Sciences. 2008; 2(1): 10.

[14] Pushparaj T, Ramabalan S. Influence of CNSL biodiesel with ethanol additive on diesel engine performance and exhaust emission. International Journal of Mechanical Engineering and Technology (IJMET). 2012; 3(2), 665 – 674

[15] Devarajan Y, Munuswamy DB, Radhakrishnan S, Mahalingam A, Nagappan B. Experimental Testing and Evaluation of Neat Biodiesel and Heptanol Blends in Diesel Engine. Journal of Testing and Evaluation, 2018 ;47(2):20170307. http://dx.doi.org/10.1520/jte20170307

[16] Devarajan Y, Munuswamy DB, Mahalingam A, Nagappan B. Performance, Combustion, and Emission Analysis of Neat Palm Oil Biodiesel and Higher Alcohol Blends in a Diesel Engine. Energy & Fuels. 2018; 12. doi.org/10.1021/acs.energyfuels.8b01125

[17] Venkata Ramanan, M, Yuvarajan, D, Emission analysis of preheated methyl ester on CI engine. Appl. Mech. Mater. 2015; 812: 21-25.

[18] H Behera P, Murugan S, Nagarajan G. Dual fuel operation of used transformer oil with ethyne in a DI diesel engine. Energy Conversion and Management. 2014; 87:840–7.

[19] Brusca S, Lanzafame R, Garrano AMC, Messina M. On the possibility to run an internal combustion engine on ethyne and alcohol. Energy Procedia. 2014; 45:889–98.

[20] Puranam SV, Steeper RR. The Effect of Ethyne on Iso-octane Combustion in an HCCI Engine with NVO. SAE International Journal of Engines; 2012;5(4):1551–60.

[21] Arul Gnana Dhas A, Devarajan Y, Nagappan B. Analysis of emission reduction in ethyne–biodiesel-aspirated diesel engine. International Journal of Green Energy. 2018 ;15(7):436–40.

[22] Abdul Majid Z, Mohsin R, Shihnan AH. Engine Performance And Exhaust Emission Of Diesel Dual Fuel Engine Fuelled By Biodiesel, Diesel And Natural Gas. Jurnal Teknologi; 2016 ;78(6).

[23] Majid ZA, Mohsin R, Nasri NS. Effect of Bioethanol on Engine Performance and Exhaust Emissions of a Diesel Fuel Engine. International Journal of Technology; 2016 ;7(6):972.

[24] Mohsin R, Majid ZA, Shihnan AH, Nasri NS, Sharer Z. Effect of biodiesel blends on engine performance and exhaust emission for diesel dual fuel engine. Energy Conversion and Management; 2014;88:821–8.

[25] Mohsin R, Yaacob Z, Abdul Majid Z, Ashraf S. Inherent Fuel Consumption and Exhaust Emission of the CNG–Petrol Bi–Fuel Engine Based at Non–Loaded Operation. Jurnal Teknologi; 2008:48(1).

[26] Supee A, Mohsin R, Majid ZA, Raiz MI. Effects of Compressed Natural Gas (CNG) Injector Position on Intake Manifold towards Diesel-CNG Dual Fuel (DDF) Engine Performance. Jurnal Teknologi; 2014:70(1).

[27] Supee A, Shafeez MS, Mohsin R, Majid ZA. Performance of Diesel-Compressed Natural Gas (CNG) Dual Fuel (DDF) Engine via CNG-Air Venturi Mixjector Application. Arabian Journal for Science and Engineering 2014: 39(10):7335–44.

[28] Devarajan Y, Munuswamy DB, Nagappan B, Pandian AK. Performance, combustion and emission analysis of mustard oil biodiesel and octanol blends in diesel engine. Heat and Mass Transfer, 2018; 17;54(6):1803–11. http://dx.doi.org/10.1007/s00231-018-2274-x

[29] Pandian AK, Munuswamy DB, Radhakrishanan S, Devarajan Y, Ramakrishnan RBB, Nagappan B. Emission and performance analysis of a diesel engine burning cashew nut shell oil bio diesel mixed with hexanol. Petroleum Science, 2018;15(1):176–84. http://dx.doi.org/10.1007/s12182-017-0208-8

[30] Schirmer WN, Gauer MA, Tomaz E, Rodrigues PRP, de Souza SNM, Chaves LI, et al. Power generation and gaseous emissions performance of an internal combustion engine fed with blends of soybean and beef tallow biodiesel. Environmental Technology, 2015;37(12):1480–9. Available from: http://dx.doi.org/10.1080/09593330.2015.1119202

[31] Petenucci ME, Fonseca GG. Production, characterization, and evaluation of the stability of biodiesel obtained from greasy agroindustrial waste during storage. Environmental Technology, 2016;38(10):1255–62. http://dx.doi.org/10.1080/09593330.2016.1225126

[32] Bedogni GA, Acevedo MD, Aguzín F, Okulik NB, Padró CL. Synthesis of bioadditives of fuels from biodiesel-derived glycerol by esterification with acetic acid on solid catalysts. Environmental Technology , 2017;39(15):1955–66. Available from: http://dx.doi.org/10.1080/09593330.2017.1345986

[33] Barik D, Murugan S, Sivaram NM, Baburaj E, Shanmuga Sundaram P. Experimental investigation on the behavior of a direct injection diesel engine fueled with Karanja methyl ester-biogas dual fuel at different injection timings. Energy, 2017 ;118:127–38. Available from: http://dx.doi.org/10.1016/j.energy.2016.12.025

[34] Suresh Babu Rao H, Venkateswara Rao T, Hemachandra Reddy K. Influence of injection timing on cerium oxide nanoparticle doped in waste cooking palm oil bio-diesel and diesel blends fuelled in diesel engine. International Journal of Ambient Energy, 2018;1–6.

[35] Srivastava AK, Soni SL, Sharma D, Sonar D, Jain NL. Effect of compression ratio on performance, emission and combustion characteristics of diesel–acetylene-fuelled single-cylinder stationary CI engine. Clean Technologies and Environmental Policy , 2017;19(5):1361–72.

[36] Appavu P, Venkata Ramanan M. Study of emission characteristics of a diesel engine using cerium oxide nanoparticle blended pongamia methyl ester. International Journal of Ambient Energy [Internet]. Informa UK Limited; 2018 May 25;1–4. Available from: http://dx.doi.org/10.1080/01430750.2018.1477063

Taylor & Francis
Taylor & Francis Group

Materials Research Innovations

ISSN: 1432-8917 (Print) 1433-075X (Online) Journal homepage: https://www.tandfonline.com/loi/ymri20

Effect of flame-retardant additive with polyurea for explosive environment

Arunkumar T, Venkatachalam P, Anish. M, Beemkumar N., Jayaprabakar J. & Sajin J B

To cite this article: Arunkumar T, Venkatachalam P, Anish. M, Beemkumar N., Jayaprabakar J. & Sajin J B (2019): Effect of flame-retardant additive with polyurea for explosive environment, Materials Research Innovations, DOI: 10.1080/14328917.2019.1700331

To link to this article: https://doi.org/10.1080/14328917.2019.1700331

MATERIALS RESEARCH INNOVATIONS
https://doi.org/10.1080/14328917.2019.1700331

Taylor & Francis
Taylor & Francis Group

Effect of flame-retardant additive with polyurea for explosive environment

Arunkumar T[a], Venkatachalam P[b], Anish. M[c], Beemkumar N.[d], Jayaprabakar J.[c] and Sajin J B[e]

[a]Department of Mechanical Engineering, CMR Institute of Technology, Bengaluru, India; [b]Department of Mechanical Engineering, MVJ College of Engineering, Bengaluru, India; [c]School of Mechanical Engineering, Sathyabama Institute of Science and Technology, Chennai, India; [d]Department of Mechanical Engineering, Jain University, Bengaluru, India; [e]Department of Mechanical Engineering, Sree Buddha College of engineering, Pattoor Kerala, India

ABSTRACT

The demand for improved damage control materials to address fire mitigation has led to an interest in polyurea (PU). The main problem with PU is poor burning properties which produce smoke to the environment and threaten public health. In order to improve its fire characteristics, PU may be mixed with flame-retardant (FR) additives. Melamine polyphosphate (MPP) is an FR additive which is a halogen-free compound and possesses high thermal stability. In this work, FR and thermal property of PU, with and without the addition of MPP (0%, 5%, 10% and 15% by weight), was studied using flammability, limiting oxygen index, smoke density and thermogravimetric analysis as per American Society for Testing and Materials standards. The results indicate that 10% and above quantities of MPP with PU have excellent FR, low heat release rate and smoke suppression efficiency.

ARTICLE HISTORY
Received 23 August 2019
Accepted 23 October 2019

KEYWORDS
Polyurea; FR additive; LOI; smoke density; explosive environment

Introduction

In response to the extensive demands at national and global levels, liquid storage tanks are designed so as to avoid environmental pollution. For those demands, liquid storage tank under the harsh environment has always been a felt need and of great interest to the researchers and scientists [1]. The storage tanks usually store oil, diesel, biodiesel, liquid hydrogen, industrial chemicals, petroleum products, etc. These applications are at risk of fire and explosion due to leakage, fire hazards, etc. Explosion is a catastrophic failure causing environmental pollution which threatens public health and leads to society hazard [2]. To overcome these kinds of explosion scenarios, hazardous liquid storages to be protected with suitable materials having flame resistance, low smoke density, toxicity, heat release, etc. The novel polyurea (PU) is replacing traditional materials such as metals and ceramics even in an explosive environment. PU is an intense material from polymer family derived from isocyanate and amine; it has desirable properties such as rapid curing, high bonding strength, no volatile organic compounds, chemical resistance and excellent mechanical properties [3–6]. PU is widely used in explosive applications such as aerospace, defence, marine, chemical, oil and gas industries and hydrogen liquid storages [7–10]. Despite their many qualities, the effectiveness of PU is incomplete in the above-mentioned applications due to ignitability, slight toxicity and rapid heat release [11–13]. In order to reduce the rate of burning, one of the envisioned solutions involves enhancing the fire-retardant abilities of the existing PU. Unfortunately, most of the flame-retardant (FR) additives are being discarded from commercial usage due to their persistence, toxic nature, bioaccumulation, human health and other environmental issues [14,15]. Likewise, the accumulation of FR additives with PU is becoming a serious problem due to increased smoke discharge while burning. To overcome this issue, PU is necessary to blend with suitable FR additives like melamine polyphosphate (MPP) in precise quantities. However, FR additive blended with commercial PU inventions has not been elucidated in the open literature [16]. The present work focuses on the elucidation of the effect of MPP with PU by conducting thermal analyses to understand the thermal degradation and the fire-retardant properties. The thermogravimetric analysis (TGA) is carried out (fall of peak heat release rate [HRR]) to identify the effective proportion of MPP with PU. MPP is the FR additive chosen because it does not need other chemical elements to the system, and their mode of action compliments the polymers. The novelty of this work is to explore the precise quantities of MPP FR additives with PU to understand the thermal degradation and the fire-retardant properties.

Materials and methods

The FR-PU samples were prepared in a beaker by mixing the various percentages of MPP (0%, 5%, 10% and 15% by weight) in the diamine oligomer; a homogeneous mixture was attained by using a high-speed mechanical stirrer. Then, isocyanate was added to the beaker with vigorous stirring for 30 s and then poured the mixture into an aluminium mould. The amount of isocyanate required for the reaction with diamine was calculated from the equivalent weight of diamine. Some excess quantity of isocyanate index (1.20) was used to avoid the chattels loss from environmental factors like humidity [17]. The readied PU samples were cured at room temperature for 12 h and afterwards kept in an oven at 80°C for 24 h to complete curing [18]. In this work, four different samples were prepared including pure PU and PU blended with 5% MPP, PU blended with 10% MPP and PU blended with 15% MPP by weight which will here forth be referred as PU, PU + 5% MPP, PU + 10% MPP and PU + 15% MPP, respectively. Flammability testing was done by horizontal burning and vertical burning method as per American Society for Testing and Materials (ASTM) D635 on standard specimen of dimension 125 × 12.7 × 3.2 mm by ATLAS 18-3918. Flammability rate of the sample is calculated using Equation (1).

CONTACT Arunkumar T arunkumar.t@cmrit.ac.in Department of Mechanical Engineering, CMR Institute of Technology, Bengaluru, India

$$\text{Flammability or Burning rate}\left(\frac{\text{mm}}{\text{miniute}}\right) = \frac{\text{L}}{\text{T}} \quad (1)$$

L = Length of the burnt part in mm (75 mm, i.e. 25–100 mm); T = Time taken for burnt length L in minute. The limiting oxygen index (LOI) testing is one of the methods to determine the relative flammability of polymeric materials [19]. LOI is the amount of oxygen needed in the atmosphere to support combustion. The LOI test was carried out using a Stanton Red croft Model FTA-I apparatus as per ASTM D2863 as a specimen of dimension 26.4 mm × 26.4 mm × 6 mm. Smoke density testing is one of the widely used testing methods for observing and measuring the relative density of smoke produced by burning materials [20]. The test was carried out by SDAS Model SSI516 apparatus as per ASTM D2843 standard dimension of 26.4 × 26.4 × 6 mm. Thermogravimetric (TG) and differential scanning calorimetry has been carried out simultaneously in STA 449 F1 Jupiter® instruments as per ASTM E1131 under nitrogen gas at 10°C/min of heating rate over the 50–800°C temperature range. The specimen is taken 10–15 mg and placed in the crucible. All the measurements were repeated three times to ensure good reproducibility of the results.

Results and discussion

Flammability test

Horizontal and vertical flammability testing was carried out to determine the comparative burning rate/resistance of PU, PU + 5% MPP, PU + 10% MPP and PU + 15% MPP. The horizontal and vertical burning rate of the PU with and without of MPP is presented in Table 1, and Figure 1 has shown that the burning rate is reduced with the increase in MPP content from 5% to 15%. Also, increasing MPP, the mass and size of the drops decreased due to increased drop viscosity and decreased melamine sublimation rate. In horizontal test, the burning rate of the PU + 5% MPP sample is 3% reduced from PU. However, burning rate of the PU + 10% MPP and PU + 15% MPP samples is reduced 12% and 23%, which is a noteworthy effect. Similarly, in vertical test, burning rate of the PU + 5% MPP, PU + 10% MPP and PU + 15% MPP samples was reduced 9%, 18% and 28%, respectively. The elapsed time for the horizontal sample is greater than the vertical sample due to upward fire propagation. As a result, 5% of MPP with PU gives no significant improvement in burning rate in both horizontal and vertical tests. However, 10% and 15% of MPP were sufficient to bring superior fire retardancy. Overall, the synergistic effect of MPP in PU is due to chemical bonding between the components facilitating the lower burning rate [21].

Limiting oxygen index test

All the samples at the starting indicated some similar characteristics like no charring and dripping. These samples are erratic burning in nature, and a steady glow was observed when it is ignited. The percentages of the oxygen index value at normal room temperature (25°C) of the PU + MPP samples were extremely varied from PU as presented in Table 1. The LOI value of PU is 23% when MPP is added into PU, and the LOI value of PU improved significantly. Furthermore, the FR MPP-blended PU, i.e. PU + 5% MPP, PU + 10% MPP and PU + 15% MPP, increases the LOI 8.6%, 30% and 39%, respectively. It is well known that when LOI <20%, it is 'self-burning material'; when LOI >28%, it is 'self-extinguishing material'; and when 20%< LOI <28%, it is 'slow-burning material'. The pure PU has 23% which is stated that PU has slow-burning material. As a result, less than 5% of MPP in PU gives no significant improvement in LOI. However, 10% and above amount of MPP was

Table 1. Horizontal and vertical burning rate of the PU with and without of MPP.

		Horizontal		Vertical		
Sample	Burned length 'L' (mm)	Elapsed time 'T' (seconds)	Burning rate (mm/min)	Elapsed time 'T' (seconds)	Burning rate (mm/min)	LOI %
PU	75	230	19.56	129	34.88	23
PU + 5% MPP	75	238	18.90	142	31.69	25
PU + 10% MPP	75	264	17.04	158	28.48	30
PU + 15% MPP	75	300	15	181	24.86	32

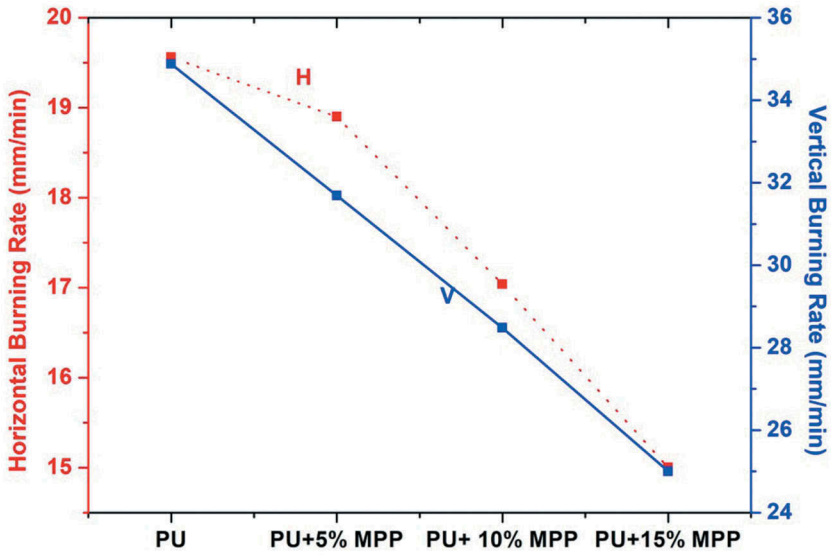

Figure 1. Burning rate of PU and MPP-blended PU.

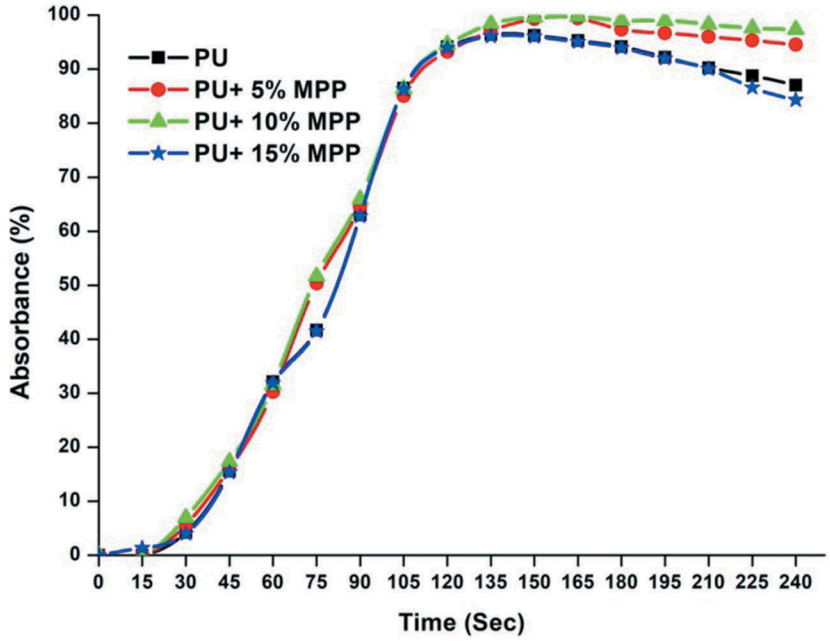

Figure 2. Absorbance per cent of PU and MPP-blended PU.

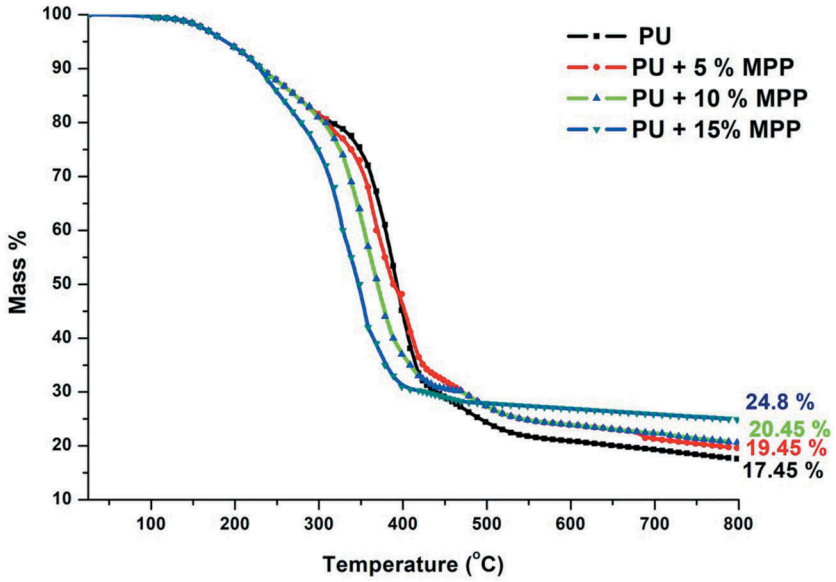

Figure 3. TGA of PU and MPP-blended PU.

sufficient to bring superior fire retardancy and enhanced to self-extinguishing material category.

Smoke density test

Measurements were made in terms of loss of light transmittance through a collected volume of smoke. All the samples' exit sign is visible throughout the test. Initially, average absorbance per cent is gradually increased, and then, it has reached maximum at the time of 135 s as shown in Figure 2. The absorbance % of PU, PU + 5% MPP and PU + 10% MPP samples were the same nature when reaching the peak. However, PU + 15% MPP is slightly diverged and decreased the absorbance percentage from PU which means a higher amount of MPP produces heavier smoke. The smoke density ratings of the PU, PU + 5% MPP, PU + 10% MPP and PU + 15% MPP are 62.10%, 65.85%, 67.10% and 61.62%, respectively; it has been calculated from area in under the absorption curve.

Thermal stability

The thermal degradations of PU and MPP-blended PU samples were studied to understand the combustion behaviour. The thermal stability of PU + 10% MPP and PU + 15% MPP samples was decreased than PU due to more phosphorus content in a higher quantity of MPP as shown in Figure 3. At 10% mass loss ($T_{10\%}$ °C) for all samples, there is no significant change in temperature. The 20% mass loss ($T_{20\%}$ °C) and maximum degradation temperature (T_{max}) of samples are shown in Table 2. However, at high temperature (800°C), all MPP-blended PU retains higher char residue than PU.

Table 2. Thermal property and char residue of PU and MPP-blended PU.

Sample	$T_{20\%}$ °C	T_{max} °C	Char at 800°C, %
PU	318	430	17.45
PU + 5% MPP	308	440	19.45
PU + 10% MPP	298	415	20.45
PU + 15% MPP	278	400	24.8

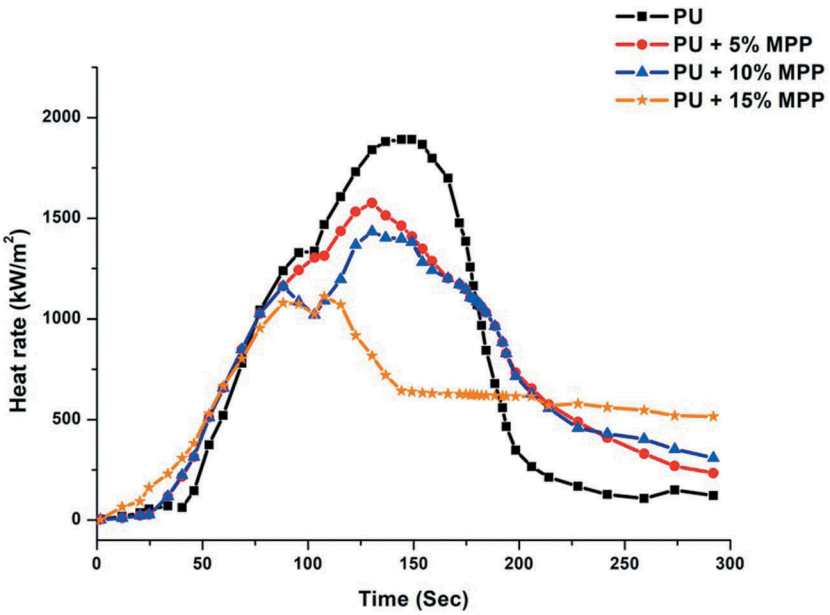

Figure 4. Heat release effect of PU and MPP-blended PU.

The entire sample has two-step heat release and is shown in Figure 4. The results revealed that MPP caused a change in the HRR during the burning of PU. Interestingly, for MPP-blended PU, decrease in HRR was observed which can be the result of a synergistic effect between the FR additives [22]. In comparison with PU that contains MPP FR, generous decrease in the peak HRR was observed for all the compositions. The peak HRR of PU, PU + 5% MPP, PU + 10% MPP and PU + 15% MPP is 1891 ± 42, 1575 ± 56, 1433 ± 61 and 1068 ± 39 kW/m^2, respectively. The PU + 15% MPP HRR is 43% reduced from PU; it is indicated that 10% and above MPP is extremely supporting the FR's action.

Conclusion

This work explored the precise quantities of MPP FR additives with PU to understand the thermal degradation and the fire-retardant properties. The burning rate is reduced with the increase in MPP content from 5% to 15%. During limiting oxygen test, all the samples have anxious properties such as severe shrinkage, erratic burning, dripping, no charring and afterglow. As a result, less than 5% of MPP in PU gives no significant improvement in LOI. However, 10% and above amount of MPP was sufficient to bring superior fire retardancy and enriched the PU as self-extinguishing material. All the smoke density rating values were maintained at a level (62.09–65.70%). This is revealed that the addition of MPP with PU is not influenced the smoke discharge while burning. Furthermore, at high temperature (800°C), all MPP-blended PU retains higher char residue than PU. All these results indicate that the 10% and above quantities of MPP with PU have excellent FR and smoke suppression efficiency. To sum up, the MPP is an efficient halogen-free FR for PU, suggesting that the good dispersibility and compatibility of MPP have improved the flame retardancy of PU.

Disclosure statement

No potential conflict of interest was reported by the authors.

Notes on contributors

Arunkumar T Indian citizen, born in Gingee, Villupuram District, TamilNadu. He is specialized in the field of Mechanical Engineering, with his Bachelor Degree in Mechanical Engineering, Master Degree in Engineering Design and PhD in Mechanical engineering (Coating). He has 10 years of teaching experience and is currently working as an Associate Professor in the Department of Mechanical Engineering, CMR Institute of Technology, Bengaluru, India. His research interests cover ceramic, polymeric, nano materials, surface coating, tribological behaviour, corrosion, and mechanical testing. He as a co-investigator has successfully completed a funded research project from the Ministry of Defense, CVRDE, Chennai, India. He has published more than 20 research articles in various SCI/WoS and Scopus indexed Journals.

Venkatachalam P is specialized in the field of Materials Science, with his Bachelor Degree in Physics, Master Degree in Materials Science and PhD in Metallurgical and Materials Engineering. He has 12 years of teaching experience and is currently working as an Associate Professor in the Department of Mechanical Engineering, MVJ College of Engineering, Bengaluru, India. His research interests are severe plastic deformation processes, texture engineering and structure property correlations. He completed one sponsored project funded by DST, New Delhi under fast track scheme for young scientist.

Anish. M has obtained his Bachelor's degree in Mechanical Engineering, Master's degree in Thermal Engineering and PhD in Nuclear Reactor. He has more than 08 years of teaching experience at various levels and is presently working as an Assistant Professor in the Department of Mechanical Engineering, Sathyabama Institute of science and Technology, Chennai, TamilNadu, India. He has guided a good number of Academic Projects for UG and PG students in his career. He has published/presented several papers in various national and international journals / conferences.

Beemkumar N. has obtained his Bachelor of Engineering in Mechanical Engineering, Master of Engineering in Energy Engineering and Ph.D. in Solar Thermal Energy Storage. He has more than 13 years of teaching experience. He has published more than 50 research articles in various SCI/WoS and Scopus indexed Journals with the cumulative impact factor closer to 45 (As per Journal Citation Reports ® Clarivate Analytics). He received many awards for his outstanding contribution in the research. His current research interests include Thermal energy storage with nano-encapsulated PCM, methods to reduce NOx emission in bio-fuelled CI engine and solar powered refrigeration systems.

Jayaprabakar J. is a citizen of India, born in Gudiyattam, Vellore District, TamilNadu. He obtained his Bachelor's degree in Mechanical Engineering Master's degree in Thermal Engineering and PhD in Alternate fuels. He has more than 16 years of teaching experience at

various levels and is presently working as an Associate Professor in the Department of Mechanical Engineering, Sathyabama Institute of science and Technology, Chennai, India. He has completed a funded project and is currently involving in a few funded projects. Currently 4 research scholars are pursuing PhD under his guidance. He has guided a good number of Academic Projects for UG and PG students in his career. He has published/presented several papers in various national and international journals / conferences.

Sajin J B is presently working as an Associate Professor in Sree Buddha college of Engineering, Pattoor, Kerala. He acquired B.Tech in Mechanical Engineering and ME in Manufacturing and PhD in Advanced composite materials. He has 10 years of teaching experience and published more than 15 research papers in various International and National journals. His research interest covers composite materials, bio-composites, Nanomaterial's and bio diesel.

ORCID

Arunkumar T http://orcid.org/0000-0003-4425-2878
Beemkumar N. http://orcid.org/0000-0003-3868-0382
Jayaprabakar J. http://orcid.org/0000-0003-3290-5771

References

[1] Arunkumar T, Sunitha S, Theerthagiri J, et al. Effect of polyurea coating on corrosion resistance over mild steel and aluminium substrates for liquid storage applications. Mol Cryst Liq Cryst. 2018 Jul;670(1):60–73.
[2] Chang I, Lin -C-C. A study of storage tank accidents. J Loss Prev Process Ind. 2006 Jan;19(1):51–59.
[3] Arunkumar. T, Ramachandran S. Analysis of hardness of polyurea coated on mild steel with effect to fuel absorption. Int J Appl Eng Res. 2015;10(11), 10415–10418.
[4] Broekaert M. Polyurea spray coatings: the technology and latest developments. European Coatings Conference'02, Berlin, Germany, 2002.
[5] Arunkumar. T, Ramachandran S. Adhesion behavior of polyurea coating on mild steel. Int J Appl Eng Res. 2015;10(1):1143–1149.
[6] Arunkumar T, Ramachandran S. Surface coating and characterisation of polyurea for liquid storage. Int J Ambient Energy. 2016 Aug;38 (8):781–787.
[7] Arunkumar. T, Ramachandran S. Thermal and fire retardant behaviour of polyurea. Int J Appl Eng Res. 2015;10(1),10159–10162.
[8] Pandey S, Rath SK, Samui AB. Structure–thermomechanical property correlations of highly branched siloxane–urethane networks. Ind Eng Chem Res. 2012 Feb;51(9):3531–3540.
[9] Mikroyannidis JA. Synthesis and thermal characteristics of phosphorus-containing polyureas and copolyureas based on 1-[(dialkoxyphosphinyl)methyl]-2,4- and −2,6-diaminobenzenes. J Polym Sci. 1984 Nov;22(11):3423–3437.
[10] Arunkumar T, Ramachandran S. Investigation of morphological and mechanical features of polyurea. Appl Mech Mater. 2015 Jun;766–767:606–611.
[11] Arunkumar T, Ramachandran S, Muthumanickam MA, et al. Study of surface roughness analysis of polyurea coating. J Balkan Tribological Assoc. 2016;22(4):3528–3537.
[12] Ramachandran S, Arunkumar MS. Comparative dynamic analysis on coated aluminium and mild steel plate under projectile impact by Abaqus explicit method. Int J Appl Eng Res. ISSN 0973-4562. 2015;10(13), 11012–11017.
[13] Jun Zhang ME, Horrocks AR. The flammability of polyacrylonitrile and its copolymers I. The flammability assessment using pressed powdered polymer samples. J Fire Sci. 1993 Sep;11(5):442–456.
[14] Hobbs C. Recent advances in bio-based flame retardant additives for synthetic polymeric materials. Polymers. 2019 Jan;11(2):224.
[15] Morgan AB. The future of flame retardant polymers – unmet needs and likely new approaches. Polym Rev. 2018 May;59(1):25–54.
[16] Iqbal N, Tripathi M, Parthasarathy S, et al. Polyurea spray coatings: tailoring material properties through chemical crosslinking. Prog Org Coat. 2018 Oct;123:201–208.
[17] Thirumal M, Khastgir D, Singha NK, et al. Effect of a nanoclay on the mechanical, thermal and flame retardant properties of rigid polyurethane foam. J Macromol Sci Part A. 2009 May;46 (7):704–712.
[18] Cai G, Wilkie CA. Fire retardancy of polyurea and silylated α-zirconium phosphate composites with ammonium polyphosphate. J Fire Sci. 2013 Jun;32(1):35–42.
[19] Hashim R, Sulaiman O, Kumar RN, et al. Physical and mechanical properties of flame retardant urea formaldehyde medium density fiberboard. J Mater Process Technol. 2009 Jan;209 (2):635–640.
[20] Gross D, Loftus JJ, Robertson AF. Method for measuring smoke from burning materials. Symposium on Fire Test Methods—Restraint & Smoke, West Conshohocken, PA: ASTM International 1966, pp. 166–166–39.
[21] Kausar A. Thermal, mechanical and flame retardant behavior of poly(urethane-ester) nanocomposite foams reinforced with hydroxyl modified montmorillonite. Int J Plast Technol. 2015 Sep;19(2):275–287.
[22] Michalowski S, Hebda E, Pielichowski K. Thermal stability and flammability of polyurethane foams chemically reinforced with POSS. J Therm Anal Calorim. 2017 Apr;130 (1):155–163.

Trijo Tharayil
Department of Mechanical Engineering,
Sree Buddha College of Engineering,
Pattoor, Alappuzha 690529, Kerala, India
e-mail: trijotharayil@gmail.com

Neha Gitty
Department of Mechanical Engineering,
Karunya Institute of Technology and Sciences,
Coimbatore 641114, Tamil Nadu, India
e-mail: gittyneha@gmail.com

Lazarus Godson Asirvatham[1]
Department of Mechanical and
Aerospace Engineering,
Karunya Institute of Technology and Sciences,
Coimbatore 641114, Tamil Nadu, India
e-mail: godson@karunya.edu

Somchai Wongwises
Fluid Mechanics, Thermal Engineering and
Multiphase Flow Research Lab (FUTURE),
Faculty of Engineering,
Department of Mechanical Engineering,
King Mongkut's University of
Technology Thonburi,
Bangmod, Bangkok 10140, Thailand
e-mail: somchai.won@kmutt.ac.th

Effect of Filling Ratio and Tilt Angle on the Performance of a Mini-Loop Thermosyphon

The thermal behavior of a compact mini-loop thermosyphon is experimentally studied at different filling ratios (20%, 30%, 40%, 50%, and 70%) and tilt angles (0 deg, 30 deg, 45 deg, 60 deg, and 90 deg) for the heat loads of 20–300 W using distilled water as the heat pipe fluid. The presence of microfins at the evaporator results in an average decrease of 37.4% and 15.3% in thermal resistance and evaporator wall temperature, respectively, compared with the evaporator with a plain surface. Both filling ratio (FR) and tilt angle influence the heat transfer performance significantly, and the best performance of the mini-loop thermosyphon is obtained at their optimum values. The thermal resistance and thermal efficiency values lie in the ranges of 0.73–0.076 K/W and 65–88.3% for different filling ratios and tilt angles. Similarly, evaporator heat transfer coefficient and evaporator wall temperature show significant variation with changes in filling ratio and tilt angle. A combination of the optimum filling ratio and tilt angle shows a lowest thermal resistance of 0.076 K/W and a highest evaporator wall temperature of 68.6 °C, which are obtained at 300 W. The experimental results recommend the use of mini-loop thermosyphon at an optimum filling ratio for electronics cooling applications, which have a heat dissipation of 20–300 W. [DOI: 10.1115/1.4043464]

Keywords: loop thermosyphon, filling ratio, tilt angle, distilled water, flat evaporator, flattened heat pipe

1 Introduction

The need for efficient cooling methodologies is increasing day by day in various applications such as nuclear reactors, internal combustion engines, gas turbine blades, air conditioners, refrigerators, rockets, solar heaters, electronic devices, etc. In electronic devices, the current flow gives rise to heat generation, and hence, the thermal management is required for improving the reliability and efficiency of the components. Miniaturization of electronic devices further enhances the importance of cooling because these devices produce large heat fluxes from a small area. Hence, the use of miniaturized electronic devices in their safe operating temperature limits still remains as a challenge.

The use of air or liquid cooling methods is not effective as far as the large fluxes from the miniaturized devices are concerned. Many researchers have already suggested heat pipes as a solution to this challenging problem because boiling and condensation in heat pipes can give rise to high heat transfer rates [1]. Miniaturized electronic devices require heat pipes of smaller size to meet the packaging constraints of these devices.

Mini-loop thermosyphon is a special kind of compact thermosyphon heat pipe that utilizes the advantages of wickless thermosyphon and separate transport lines of loop heat pipe [2]. It possesses superior advantages such as high heat transfer capability, no requirement of electricity, minimum floor area requirement, and less noise in addition to its compact size. A thermosyphon loop comprises an evaporator, vapor line, condenser, and liquid line. The vapor from the evaporator flows to the condenser where it is cooled and returns through the liquid line to the evaporator. Since no wick is used inside the heat pipe, the pressure losses can be kept to a minimum. It is also capable of transferring heat with high heat fluxes over great distances. The heat transfer depends on the heat flux, the mass flow rate of vapor, and the properties of the working fluid used in the thermosyphon loop.

A handful of investigators have worked with different designs of loop thermosyphon under various operating conditions, and these works are summarized as follows. Na et al. [3] scrutinized the heat transfer performance of a closed loop thermosyphon heat pipe used for cooling multichip cooling modules using analytical and experimental methods. The heat pipe showed a smooth change from the transient condition to a steady-state at various heat fluxes. The experimental results showed a wall superheat of 5–12 °C with a maximum heat flux of 2.5 W/cm^2. It was also observed that the condenser size is an important factor in determining the performance of the heat pipe. Gima et al. [4] conducted a heat transfer study of a loop thermosyphon having four different boiling surfaces for CPU cooling using fluorinert as the working fluid. The loop thermosyphon showed a temperature difference of 55 °C between the evaporator and ambient at the maximum heat load of 30 W. The evaporator temperature showed a decrease of 18 °C when the smooth surface was replaced by a rough surface.

Sarno et al. [5] performed thermal tests on loop thermosyphon heat pipes for cooling the seat electronics in commercial aircrafts using R141b as the heat transfer fluid for the applied heat loads of 10–100 W. The experiments were repeated at different tilts of the heat pipe. The printed circuit board of the electronic box had a maximum temperature of 88 °C at 100 W. The performance of the loop thermosyphon decreased when the tilt angle increased beyond 20 deg. Khrustalev [6] investigated the thermal performance of two loop thermosyphons having a capillary structure at evaporator in the vertical orientation using methanol and ethyl alcohol as working fluids for electronics cooling applications. The maximum heat transfer capacity of the loop thermosyphon was found to be 200 W with an evaporator temperature of 68 °C and the heat pipe reached dry out after 200 W.

[1]Corresponding author.

Contributed by the Heat Transfer Division of ASME for publication in the Journal of Thermal Science and Engineering Applications. Manuscript received May 20, 2018; final manuscript received April 3, 2019; published online May 20, 2019. Assoc. Editor: Ayyoub M. Momen.

Chang et al. [7] explored the thermal behavior of a loop thermosyphon with a thermal resistance model using water as the heat transfer fluid at different heat inputs (60–140 W) and evaporator surfaces. The experimental study showed temperature fluctuations for heat loads of 60–80 W, and it was attributed to intermittent boiling. It was also observed that the heat load is the major influencing factor on the thermal performance. Chehade et al. [8] examined the thermal behavior of a loop thermosyphon heat pipe in a heat flux range of 4.6–13.9 W/cm^2 at different filling ratios, condenser coolant inlet temperature, and flow rates. The experimental results showed that the optimum filling ratio was in between 7% and 10%, and the optimum values of coolant temperature and flow rate were 5 °C and 0.7 l/min, respectively.

Franco and Filippeschi [9] reviewed the research works in the loop thermosyphon and compared the different designs. It was observed that there is a considerable variation in the experimental results. This review paper highlighted the need for further experimental research in loop thermosyphon to have a better understanding of the heat transfer phenomenon. Zhang et al. [10] conducted a visual experimental study and compared the heat transfer characteristics of a two-phase loop thermosyphon using water and ethanol as working fluids. Results showed higher thermal resistances with ethanol as the working fluid. It was also reported that the performance can be improved with larger temperature difference, optimum filling of working fluid, and lower flow resistance. Gualous et al. [11] analyzed the heat transfer behavior of a loop thermosyphon using water as a working fluid in a heat flux range of 1–14 W/cm^2 and compared the heat transfer coefficient values at evaporator and condenser with the correlations. A new correlation was also developed, and it showed a variation of ±10% with the experimental data.

Similarly, a few researchers have used nanofluid and other boiling enhancement techniques in various heat pipes including loop thermosyphon to enhance the heat transfer [12–23]. It can be concluded that loop thermosyphon is still an active area of research, and most of the previous works in loop thermosyphon has been done with low heat loads (less than 200 W) or low heat fluxes (less than 15 W/cm^2). So, a design satisfying higher heat loads or heat fluxes is necessary to meet the present and future electronic cooling requirements. Similarly, only very few researchers have studied the effect of an inclination of mini-loop thermosyphon on the heat transfer performance, and more experimental studies are required to fully understand the heat transfer mechanism. The heat transfer study at various inclinations is important because many applications such as electronics in aircraft experience the change of tilt angle of the heat pipe during their normal operation. In such situations, the decrease in performance of mini-loop thermosyphon is not acceptable.

Hence, in the present study, a mini-loop thermosyphon heat pipe having microfins at the evaporator surface and flattened transport lines is designed, and its heat transfer performance is analyzed with the use of distilled water as the heat pipe fluid in a heat load range 20–300 W (5–75 W/cm^2). The experiments are conducted at different filling ratios to optimize the filling ratio (FR), and the heat transfer study is also extended at various inclinations of the mini-loop thermosyphon ranging from 0 deg to 90 deg. Filling ratio is the ratio of the amount of working fluid filled into the loop thermosyphon to the total inside volume of the loop thermosyphon.

2 Experimentation

2.1 Details of the Mini-Loop Thermosyphon. The mini-loop thermosyphon consists of five parts namely: evaporator, reservoir, condenser, riser (vapor line), and downcomer (liquid line) as shown in Fig. 1(*a*). The complete details of the mini-loop thermosyphon elements are given in Table 1. All the parts of the mini-loop thermosyphon are made of copper. The evaporator is square in shape and has a dimension of 20 mm × 20 mm. The evaporator also consists of 18 microfins having a thickness of 0.5 mm, height of 1 mm, and length of 19 mm on the inner surface of the evaporator as shown in Fig. 1(*b*). These fins act like a capillary structure and also help in increasing heat transfer area and liquid supply to the evaporator. The presence of fins at the evaporator also helps in preventing reverse movement of vapor through the downcomer by increasing the vapor generation rate at the evaporator. A flat evaporator is considered in this study because it offers lower contact resistance with the heater. The evaporator wall has a uniform thickness of 1 mm throughout, and it is capable of withstanding the inside vapor pressure even at high heat inputs (up to 300 W). The reservoir stores and supplies the working fluid to the evaporator and makes sure that sufficient liquid is always available at the evaporator even at high heat loads.

Flattened copper pipes are used as transport lines in this mini-loop thermosyphon, and they are used to reduce the overall thickness of the mini-loop thermosyphon in the horizontal orientation. The dimensions of the transport lines are uniform throughout from the evaporator outlet to the reservoir inlet. The flattened copper pipes are prepared by uniformly pressing the bent circular copper pipe using a mechanical press. The flattening process is done slowly and with extreme care to ensure uniform flattening of the copper pipe. The components of the heat pipe are chemically cleaned to remove the oily impurities from inner surfaces before assembling them. The transport lines are joined to the evaporator and reservoir section by the brazing process.

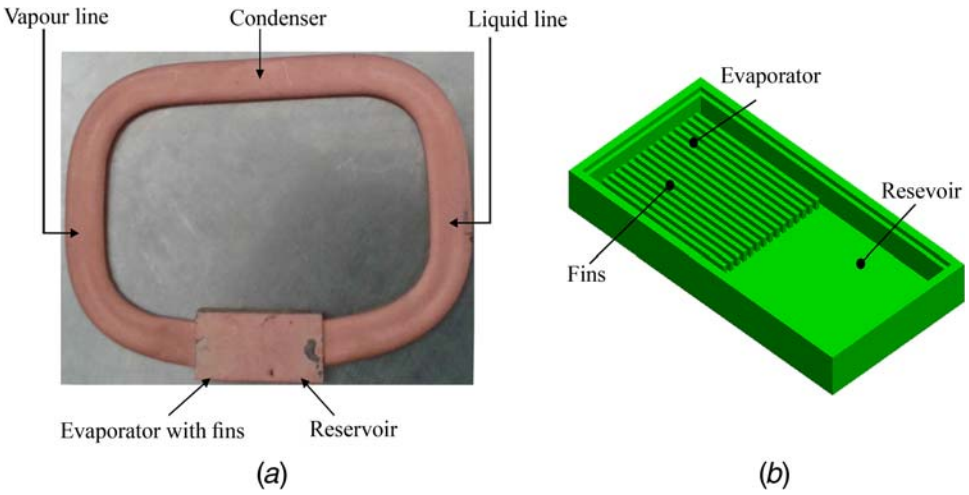

Fig. 1 (*a*) Mini-loop thermosyphon and (*b*) design of the evaporator

Table 1 Details of the mini-loop thermosyphon

Specification	Dimension/Material
Working fluid	Distilled water
Filling ratios	20%, 30%, 40%, 50%, and 70%
Inclinations tested	0 deg, 30 deg, 45 deg, 60 deg, and 90 deg
Total length of the loop	342 mm
Material of the heat pipe	Copper
Evaporator	
Outer dimensions	20 mm × 20 mm
Thickness of the loop	4 mm
Heater active zone	20 mm × 20 mm
Wall thickness	1 mm
Fin dimensions	0.5 mm × 19 mm × 1 mm
Distance between fins	0.5 mm
Number of fins	18
Reservoir	
Outer dimensions	20 mm × 20 mm
Transport lines	
Inner diameter (ID)	8.5 mm
Outer diameter (OD)	9.5 mm
Height after flattening	4 mm
Length in condenser	150 mm
Condenser	
Type	Rectangular box type
Material	Acrylic
Outside dimensions	140 mm × 60 mm × 40 mm
Wall thickness	4 mm
Coolant temperature	20 °C
Coolant flow rate	20 LPH

The condenser is a rectangular container type water-cooled heat exchanger, which is prepared with acrylic sheets having a thickness of 4 mm. The size of the condenser is found to be sufficient for cooling of vapors even at high heat inputs. The water is supplied at a constant temperature and flow rate using a chilling unit and a rotameter.

Mini-loop thermosyphon undergoes a leakage check before the working fluid is filled into it. In this study, distilled water is used as the heat pipe fluid. The filling of the heat pipe fluid is done using a vacuum pumping system, and the working fluid is filled after expelling all noncondensable gases.

2.2 Experimental Setup. The experimental setup is composed of following components: mini-loop thermosyphon with the condenser, heater and hylam blocks, dimmerstat with ammeter and voltmeter, thermocouples, chilling unit, cooling water lines, pump, rotameter, data logger, and personal computer. Figure 2 represents the mini-loop thermosyphon-heater assembly. The heater comprises two cartridge heaters (each having a capacity of 200 W) fitted inside a copper slab having a square cross section in order to have a uniform temperature on the top surface of the heater. The heater is fixed in a hylam block with teflon sheets in between them. The evaporator of the mini-loop thermosyphon is placed on the heater top surface with a thermal interface paste in between them. Thermal interface paste is used to reduce the contact resistance due to small irregularities on the evaporator bottom and heater top surfaces. The assembly of heater and mini-loop thermosyphon is held tightly using a clamp attached to the hylam block. The mini-loop thermosyphon is shielded with thick thermal insulation of glass wool that blocks heat loss to ambient. The heat loss from the heater is blocked by the teflon sheets, hylam blocks, and dense layers of glass wool. The dimmerstat is used to vary the heat input to the heater, and the corresponding heat load is measured using the ammeter and voltmeter.

Figure 3 shows the position of various thermocouples on the loop thermosyphon-heater assembly along with other components of the experimental setup. Twelve T-type thermocouples, which have an accuracy of ±0.5 °C, are fixed at the heat pipe surface using an instrument welder. Two thermocouples namely (T_1 and T_2) are placed one on the heater and other at the intersection of the heater and evaporator. The evaporator temperature is measured using the thermocouple (T_3). The thermocouples (T_4 and T_5) are placed on the riser to measure the vapor line temperatures. Three thermocouples (T_6, T_7, and T_8) are placed in the condenser to measure the condenser wall temperature. Two thermocouples (T_9 and T_{10}) are placed on the downcomer to measure the temperature of the liquid coming to the reservoir. In order to supply cooling water at 20 °C to the condenser, a chilling unit is used. Similarly, the flow rate of coolant is maintained constant (20 LPH) using a pump and a rotameter. The entry of water to the condenser is from the bottom and exit is at the top, and the temperature of the water is recorded with thermocouples (T_{11} and T_{12}) at entry and exit. All thermocouple wires are attached to a data logger (Agilent 34972), which is in association with a personal computer. The temperatures recorded by the thermocouples are transferred to the computer through the data logger, and the computer stores all the temperature data for later analysis.

2.3 Experimental Procedure. Heat transfer study of the mini-loop thermosyphon is performed using distilled water as the heat pipe fluid in a heat input span of 20–300 W at dissimilar filling ratios and inclinations. First, the filling ratio of mini-loop thermosyphon is optimized by conducting experiments at filling ratios of 20%, 30%, 40%, 50%, and 70% in the vertical orientation (90 deg tilt angle). Second, the heat transfer performance is analyzed by conducting experiments at various inclinations (0 deg,

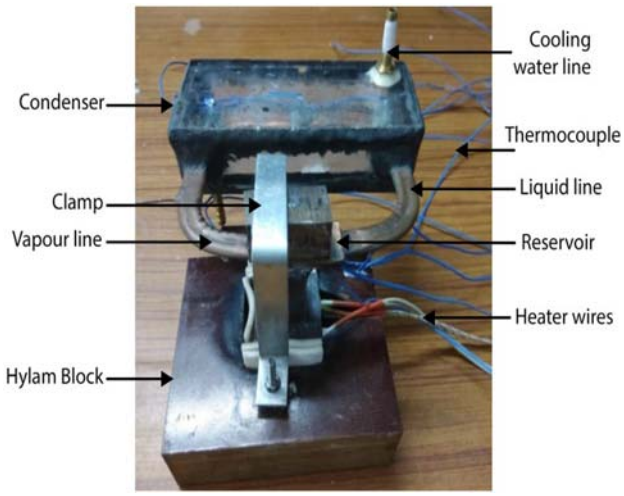

Fig. 2 Loop thermosyphon-heater assembly in the horizontal orientation (0 deg)

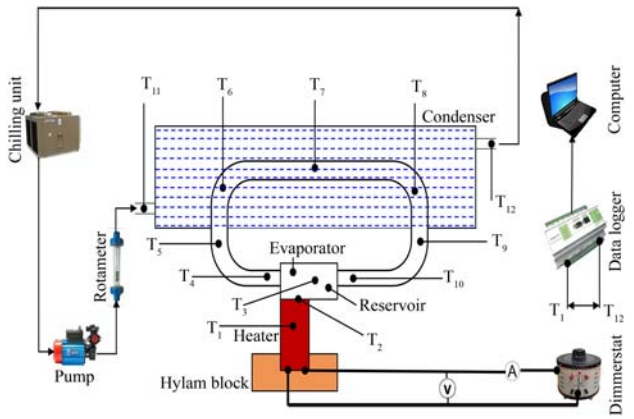

Fig. 3 Thermocouple positions along with other components of the experimental setup

30 deg, 45 deg, 60 deg, and 90 deg) for the optimum filling ratio. Figure 2 shows the horizontal orientation (0 deg) of the loop thermosyphon-heater assembly. The other orientations can be achieved by tilting the entire assembly.

The experiments are performed as follows: The mini-loop thermosyphon-heater assembly is first connected to the dimmerstat, and all thermocouples are linked with the data logger. The data logger is set to record all temperatures in every 5 s. Cooling water at 20 °C is allowed to flow through the condensers at 20 LPH, and a preliminary heat load of 20 W is applied using the dimmerstat. The mini-loop thermosyphon reaches the steady-state after a couple of minutes, and the steady-state is allowed to continue for half an hour. Then, the heat input is enhanced with a step of 40 W, and the above process is repeated. The experiment is continued in the heat load range of 20–300 W, and finally, the heat load is reduced to zero after the test with 300 W. Each experiment is repeated thrice on different days, and the mean value of readings is taken for further analysis. The thermal resistance is calculated at each filling ratio, and the optimum filling ratio is determined from the lowest thermal resistance values.

The influence of inclination angle on the thermal performance is analyzed by performing the experiments at an optimum filling ratio. The mini-loop thermosyphon-heater assembly is tilted at respective angles, and cooling water supply is maintained accordingly. Heat transfer study is conducted as described earlier for each inclination, and finally, the mini-loop thermosyphon is detached from the experimental arrangement after cooling it.

2.4 Data Reduction. The heat pipe resistance of the mini-loop thermosyphon (R_t) is the ratio of change in temperature from the evaporator to the condenser to the applied heat input, and it is calculated as in Eq. (1).

$$R_t = \frac{T_e - T_c}{Q_a} \tag{1}$$

where T_e and T_c are the evaporator and average condenser surface temperatures, respectively, and Q_a is the applied heat load.

$$T_c = \frac{T_6 + T_7 + T_8}{3}$$

$T_e = T_3$ and $Q_a = V \times I$, where V and I represent the applied voltage and current, respectively. T_6, T_7, and T_8 are the condenser wall temperatures.

Evaporator heat transfer coefficient (h_e) is the ratio of applied heat flux at the evaporator to the change in temperature from the evaporator wall to the vapor, and it is calculated using Eq. (2).

$$h_e = \frac{Q_a}{A_e(T_e - T_{ve})} \tag{2}$$

where A_e is the inside area exposed to vaporization at the evaporator and T_{ve} is the temperature of vapor at the evaporator. Since vapor temperature has not been measured separately, the first vapor line temperature (T_4) is considered as the evaporator vapor temperature.

Similarly, condenser heat transfer coefficient represents the ratio of heat rejected at the condenser to the product of the area exposed to condensation and the change in temperature from the condenser vapor to the condenser wall, and it is calculated using Eq. (3).

$$h_c = \frac{Q_c}{A_c(T_{vc} - T_c)} \tag{3}$$

where Q_c is the heat removed by cooling water at the condenser, A_c is the area available for condensation at the condenser, and T_{vc} is the temperature of vapor at the condenser. In the present work, it was not possible to fix a thermocouple to measure the vapor temperature at the condenser as the loop thermosyphon thickness was only 4 mm. It has been observed that the vapors travel fast in the vapor line, and the difference of wall temperature at the condenser inlet and vapor temperature at the condenser is almost negligible. The chance for heat loss in vapor line is also negligible as the loop thermosyphon is covered with the thick layers of glass wool insulation. Hence, the vapor line temperature near the condenser inlet (T_5) is considered as the temperature of vapor.

Thermal efficiency (η_t) of the mini-loop thermosyphon is the ratio of heat removed at the condenser to condensing liquid to the heat input at the evaporator, and it is calculated using Eq. (4).

$$\eta_t = \frac{Q_c}{Q_a} \times 100 \tag{4}$$

$$Q_c = mc(T_{12} - T_{11})$$

where m, c, T_{11}, and T_{12} denote the mass flow rate, specific heat, and inlet and outlet temperatures of cooling water at the condenser, respectively.

Effective thermal conductivity of the mini-loop thermosyphon is calculated using Eq. (5).

$$K_{eff} = \frac{L}{A_{c/s}R_t} \tag{5}$$

where $A_{c/s}$ is the outer cross-sectional area of the vapor line and L is the length of the mini-loop thermosyphon from the center of the evaporator to the center of the condenser.

2.5 Uncertainty Analysis. An experimental study is always accompanied by an uncertainty analysis because there are uncertainties associated with measuring instruments. The uncertainties in various derived parameters are calculated as given below. The heat applied at the evaporator is measured by multiplying the voltage and current readings from the voltmeter and ammeter. Hence, the uncertainty linked with the applied heat input comprises uncertainties involved in the measurements of applied voltage and current. It is calculated using Eq. (6).

$$\frac{\Delta Q_a}{Q_a} = \sqrt{\left(\frac{\Delta V}{V}\right)^2 + \left(\frac{\Delta I}{I}\right)^2} \tag{6}$$

The uncertainties of the heat pipe resistance of the mini-loop thermosyphon comprise of uncertainties in the measurement of the applied heat input (Q_a) and the temperature variation from the evaporator to the condenser (T_e–T_c). It is determined using Eq. (7).

$$\frac{\Delta R_t}{R_t} = \sqrt{\left(\frac{\Delta Q_a}{Q_a}\right)^2 + \left(\frac{\Delta(\Delta T)}{\Delta T_{ec}}\right)^2} \tag{7}$$

where ΔT_{ec} is the real temperature difference from the evaporator to the condenser. Since the heat transfer coefficient at the evaporator and the condenser is obtained from the heat input/heat rejected, corresponding heat transfer area and temperature difference, the uncertainties of the heat flux (q) and the equivalent temperature differential between the wall and vapor (ΔT_{vs}) are used to calculate uncertainty in h as in Eq. (8).

$$\frac{\Delta h}{h} = \sqrt{\left(\frac{\Delta q}{q}\right)^2 + \left(\frac{\Delta(\Delta T)}{\Delta T_{vs}}\right)^2} \tag{8}$$

The uncertainty linked with the thermal efficiency includes uncertainties in the applied heat input, mass flow rate (m) of the cooling water, and the temperature differential between the cooling water exit and entry (ΔT_w). It is determined using Eq. (9).

$$\frac{\Delta \eta}{\eta} = \sqrt{\left(\frac{\Delta Q_a}{Q_a}\right)^2 + \left(\frac{\Delta m}{m}\right)^2 + \left(\frac{\Delta(\Delta T_w)}{\Delta T_w}\right)^2} \tag{9}$$

The uncertainty analysis shows that the maximum uncertainty associated with the applied heat input, heat pipe thermal resistance, heat transfer coefficients (h_e and h_c), and thermal efficiency of mini-loop thermosyphon is 1.95%, 2.25%, 2.88%, and 3.1%, respectively.

3 Results and Discussion

3.1 Influence of Filling Ratio. The filling ratio of the mini-loop thermosyphon is optimized by conducting the experiments at the filling ratios of 20%, 30%, 40%, 50%, and 70%. Figure 4 shows the change of the heat pipe resistance of the mini-loop thermosyphon for different heat inputs ranging from 20 W to 300 W at different filling ratios. It has been observed that the thermal resistance drops when the heat input enhances from 20 W to 300 W. It is due to the rise in heat transfer from the evaporator end to the condenser end. The heat transfer from the evaporator to the condenser is relied on the vaporization rate and mass flow rate of vapor. At low applied heat inputs, the heat transfer from the heater to the evaporator is less, and there is a chance of heat loss to the reservoir because the thermal conductivity of copper is high. At higher loads, more heat is transferred to the distilled water, and it results in an increase of the vaporization rate. The increase in vaporization increases the vapor pressure that pushes the vapor to the vapor line, and it results in an increase of mass flow rate. The microfins on the inner surface of the evaporator increase the vaporization rate by providing more heat transfer area and replace the vaporized liquid immediately with the incoming liquid due to its capillary action. Since the vapor pressure is high at the evaporator side compared with the reservoir side, the reverse flow of vapor does not occur through the downcomer.

When the filling ratio increases from 20% to 30%, the thermal performance also increases, but after 30%, the thermal performance starts to decrease, which is clear from the increase in the thermal resistance. It indicates the presence of an optimum filling ratio, and it is 30% in this mini-loop thermosyphon. It can be explained as follows: at 20% FR, the amount of the heat pipe fluid is less, and when vaporization occurs, the refilling process is not sufficient to remove the heat from the evaporator. But at 30% FR, there is a necessary quantity of heat pipe fluid at all heat inputs, and it makes the removal of heat easy. When the filling ratio further increases to 40% or higher, the amount of heat pipe fluid in the mini-loop thermosyphon increases, and it results in the accumulation of the heat pipe fluid throughout the loop particularly in the evaporator. Vaporization will be fast when only a thin layer of liquid comes in contact with the hot surface. The accumulation of the liquid delays the vaporization and also affects the flow patterns that lead to low heat transfer from the evaporator region to the condenser region [24]. The capability of transferring the heat decreases with an increase of volume of working fluid, and it leads to increment in the thermal resistance. The decrease in variation of the thermal resistance at larger heat loads is because of the increased vaporization at all filling ratios.

The FR of 30% shows the lowest heat pipe resistance values at all heat inputs. The lowest heat pipe resistance is 0.076 K/W, which is obtained at the peak heat load of 300 W for the 30% FR, and it shows a reduction of 29% from the value obtained at the same heat load for 70% FR. The highest values of the heat pipe resistance are recorded at 70% FR, and it represents the accumulation of the liquid in the mini-loop thermosyphon, which disturbs the vapor formation, the mass flow rate of vapor, and the condensation phenomenon. The surplus liquid in the loop results in the deterioration of evaporation, incomplete boiling, and destruction of the flow patterns inside the mini-loop thermosyphon. At 30% FR, only sufficient quantity is available, which also helps in providing sufficient area for condensation. The condensed liquid immediately flows to the evaporator keeping the condenser surface ready for the incoming vapors.

The evaporator wall temperature depends on the rate of the heat removal from the inner surface of the evaporator. The heat removal rate relies on the FR, properties of the heat pipe fluid, thermal conductivity of the mini-loop thermosyphon material, mass flow rate of vapor, area available for vaporization, rate of condensation, etc. Figure 5 indicates the effect of FR and heat input on the evaporator wall temperature of the mini-loop thermosyphon.

It shows that the temperature of the evaporator wall enhances with increments in heat input and declines with an increase in FR until 30% FR. When FR increases above 30%, the evaporator wall temperature starts to increase for all heat loads. The optimum FR of 30% gives the maximum heat transfer from the evaporator by vaporization and immediate refilling of liquid.

Figure 5 shows that the FR plays a main part in deciding the evaporator wall temperature. For 20% FR, the insufficient amount of heat pipe fluid leads to increase in the wall temperature, and at FR above 30%, the excess liquid in the mini-loop thermosyphon affects the vaporization phenomenon. The excess fluid delays the vaporization as the supplied heat is utilized for increasing the temperature of the entire liquid in the evaporator. At higher FR, there are chances of vapor generation from both the evaporator and

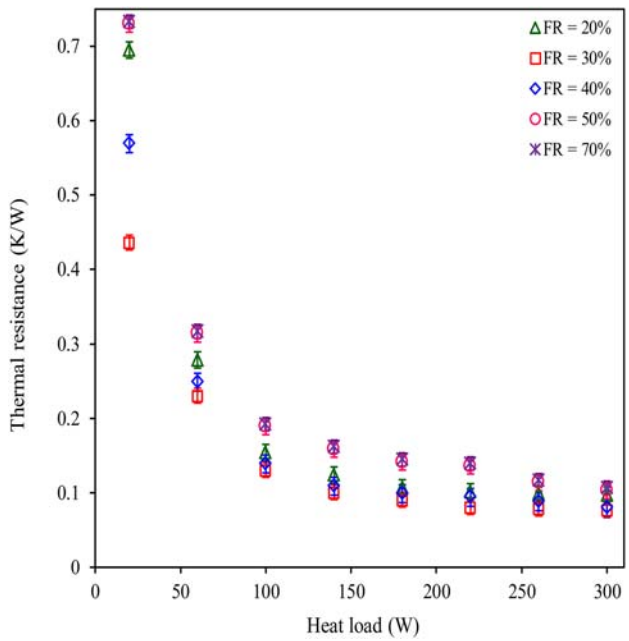

Fig. 4 Thermal resistance versus heat load (different filling ratios)

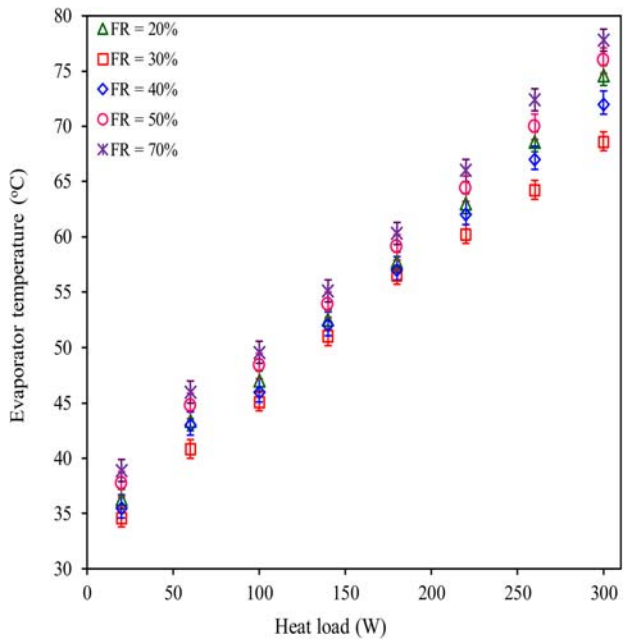

Fig. 5 Evaporator wall temperature versus heat load (different filling ratios)

reservoir. The variation evaporator wall temperature escalates with rise in the heat load for different filling ratios.

The vaporization process absorbs heat from the evaporator and fins surface and reduces the evaporator wall temperature. When steady-state is reached, the heat removal from the evaporator becomes constant as the vaporization process is constant. Since vaporization process has large heat transfer coefficient values, high rates of heat transfer are possible with this mini-loop thermosyphon. Since the thermal conductivity of copper is high, heat will be easily transferred to the inner surface of the evaporator. The capillary microfins increase the wetting phenomenon, and hence, rewetting is faster. But at higher filling ratios, the evaporator, fins, and reservoir are always filled with water, and this condition does not favor the high vapor generation [25]. The evaporator temperature varied in the range of 34.6–68.6 °C for the optimum filling ratio, and these values represent an average reduction of 9.3% compared with 70% FR. The optimum FR has the lowest temperature of 68.6 °C at 300 W, which represents a reduction of 9.2 °C from the value at 70% FR. It clearly shows that FR is an important factor affecting the thermal performance of mini-loop thermosyphon.

Figure 6 compares the heat transfer performance of the mini-loop thermosyphon having a plain and microfinned evaporator at the optimum filling ratio of 30%. It can be observed that the presence of microfins at the evaporator increases the heat transfer area, thereby reducing the thermal resistance and evaporator wall temperature. The presence of microfins also facilitates the increase of vaporization rate, and the immediate refilling of the working fluid by the fast rewetting process due to the capillary action. It also helps to prevent reverse flow through the liquid line because more vapors are generated near the vapor line. When a plain surface is used, the working fluid is spread over the entire evaporator and reservoir. This delays the vaporization process and gives rise to higher thermal resistance. The mini-loop thermosyphon with microfins shows an average decrease of 37.4% and 15.3% in thermal resistance and evaporator temperature, respectively, compared with the evaporator with the plain surface.

Figure 7 represents the change of heat transfer coefficient at the evaporator of the mini-loop thermosyphon with increases in heat inputs and filling ratios. It can be observed that the evaporator heat transfer coefficient escalates with heat load, and the variation is less at low heat inputs because of the less vapor generation rate at low heat loads. But, the value of h_e increases at higher heat inputs indicating more vapor formation and heat transfer. The vaporization is influenced by the heat transfer from the heater surface to the evaporator inner surface, area of vaporization, amount of liquid present in the evaporator, properties of the heat pipe fluid, wettability, and surface structure of the evaporator. The presence of microfins helps to enhance the available heat transfer area and assists in fast rewetting of liquid by the capillary action. The low wall thickness of the evaporator keeps the conduction resistance to a minimum value, and it helps in quick heat transfer. The evaporator heat transfer coefficient is also influenced by the number of active nucleation sites on the evaporator inner surface. The number active of nucleation sites of vaporization depends on the wall superheat that increases with the heat load. The relation of the number of nucleation sites and the wall superheat is given by Eq. (10).

$$N_a \propto N_c(1 - \cos\theta)(T_w - T_{sat})^6 \tag{10}$$

where the number of active nucleation sites and the number of microcavities on the surface are represented by N_a and N_c, respectively. Similarly, θ and $(T_w - T_{sat})$ represent contact angle and wall superheat at the evaporator surface, respectively. Since the wall superheat increases at higher heat inputs, the vaporization also increases with an increase in the number of active nucleation sites.

The value of h_e is highest for 30% FR for all heat inputs that show the influence of FR on h_e and need of right amount of working fluid in the mini-loop thermosyphon to produce the maximum heat transfer. The enhancement in the vapor formation rate increases the vapor pressure in the evaporator leading to higher vapor flow rate to the condenser. The increase in mass flow rate of vapor also directs the return of liquid to the reservoir through the downcomer. The evaporator heat transfer coefficient values do not show much variation for the 20%, 50%, and 70% filling ratios, and it indicates that insufficient and excess liquid in the mini-loop thermosyphon affect the vaporization, mass flow rate of vapor, and condensation. The highest h_e value observed is 58.6 kW/m^2 K at 30% FR, which is 36.1 kW/m^2 K greater than the value obtained at 70% FR. Even though heat loss occurs to the reservoir at all heat loads, the fast vaporization rate at 30% FR for all heat loads immediately draws liquid from the reservoir. Hence, the preheating of liquid in reservoir helps the liquid to reach the saturation temperature quickly leading to high heat transfer rates.

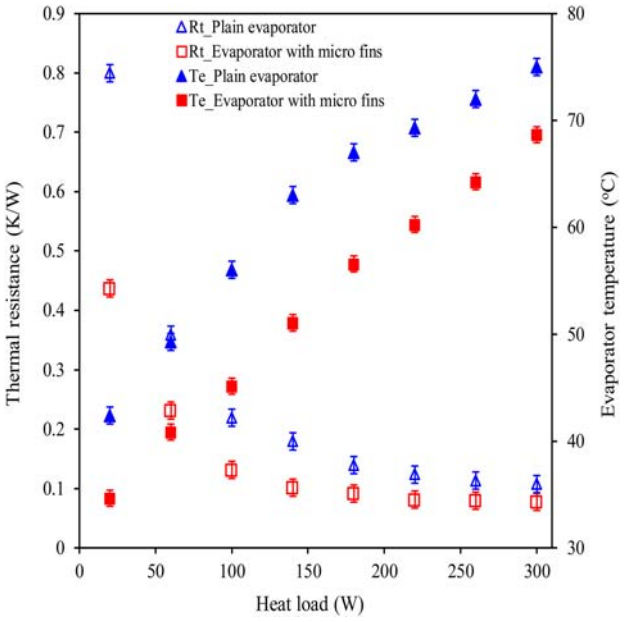

Fig. 6 Effect of microfins on the thermal performance

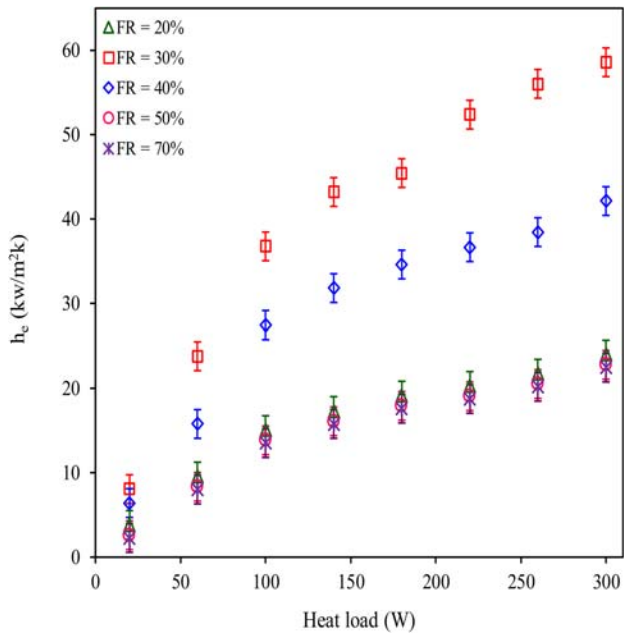

Fig. 7 Evaporator heat transfer coefficient versus heat load (different filling ratios)

The variation of thermal efficiency of the mini-loop thermosyphon with changes in heat load and filling ratio is given in Fig. 8. The thermal efficiency increases with heat load, and the optimum FR gives the maximum thermal efficiency for all heat inputs. Since the thermal efficiency depends on the heat input at the evaporator region and heat rejected at the condenser region, the high thermal efficiency values at high heat loads indicate higher heat transfer rates. The increase in mass flow rate of vapor increases the heat rejection at the condenser giving high thermal efficiency values. The thermal efficiency values lie in the range of 65–88.3% for all heat loads and filling ratios. The optimum filling ratio gives the thermal efficiency from 74% to 88.3% for heat loads of 20–300 W, and it represents an average increase of 12.2% compared with the 70% FR. The thermal efficiency values indicate that there is heat loss to the reservoir and liquid line through the mini-loop thermosyphon material and working fluid. This heat loss decreases the actual heat transferred to the condenser. Similarly, minute heat loss through the insulation to the ambient also has to be considered in thermal efficiency analysis. Hence, the thermal efficiency value is an indication of the actual amount of heat transferred from the evaporator to the condenser. The optimum FR gives the maximum thermal efficiency at all heat loads, and it represents the maximum vapor generation and heat transfer to the condenser. FR also affects the thermal efficiency because the heat removed at condenser depends on the vaporization rate, mass flow rate of vapor, and condensation process itself.

Figure 9 shows the repeatability test conducted under the same experimental settings with mini-loop thermosyphon at 30% FR for the heat loads of 20–300 W on four consecutive days. The evaporator heat transfer coefficient value is estimated on each day for various heat inputs, and these values are compared in Fig. 9. The results of the repeatability test show a maximum variation of ±2.1%, which indicate that the experimental results are repeatable.

Figure 10 compares the thermal performance of the present mini-loop thermosyphon in the vertical orientation at optimum FR with other existing loop thermosyphons available in the open literature. It is to be observed that only the thermal resistance of different loop thermosyphons is considered in this analysis. The other influencing factors like dimensions of loop thermosyphon, heat pipe fluid properties, filling ratio, coolant flow rate and temperature, etc., are not considered in this comparison. This comparison is made to emphasize that the present mini-loop thermosyphon has lower thermal resistance values compared with the existing loop thermosyphon designs in the tested heat load range. Hence, the present loop thermosyphon can be considered as a possible solution for electronics cooling applications.

3.2 Influence of Tilt Angle. Figure 11 shows the change of thermal resistance with the tilt angle of the mini-loop thermosyphon and heat input for the optimum filling ratio of 30%. Thermal resistance shows a decreasing trend with an enhancement in heat load and inclination of the mini-loop thermosyphon [31]. Since the filling ratio is the same for all inclinations, it can be observed that the inclination is also an important factor affecting the heat transfer of mini-loop thermosyphon. When the inclination increases, the

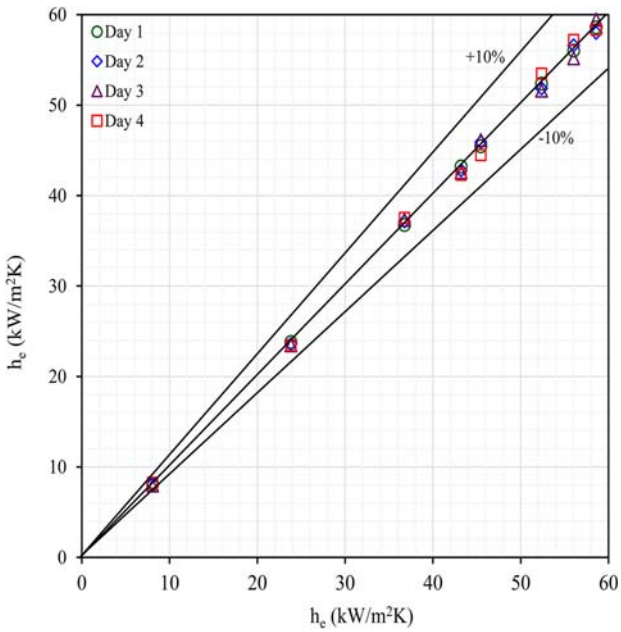

Fig. 9 Repeatability test

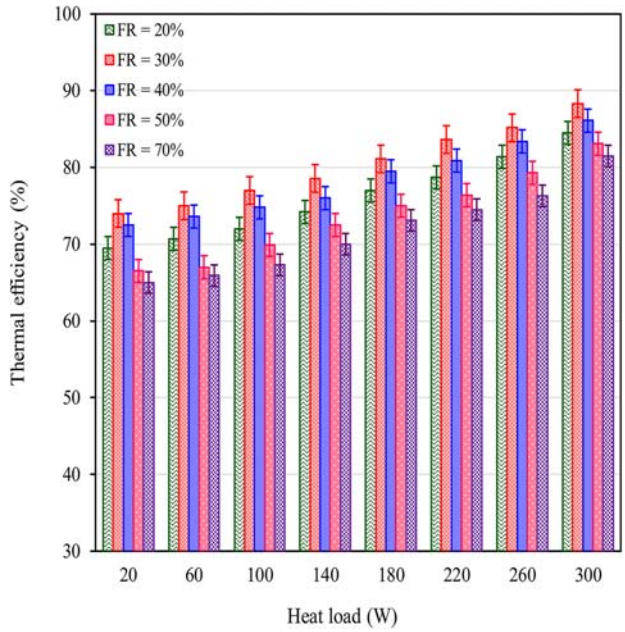

Fig. 8 Thermal efficiency versus heat load (different filling ratios)

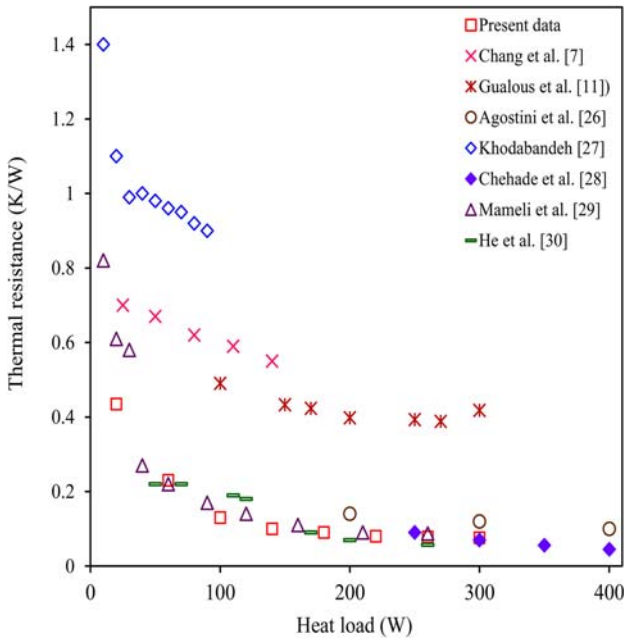

Fig. 10 Comparison of thermal resistance

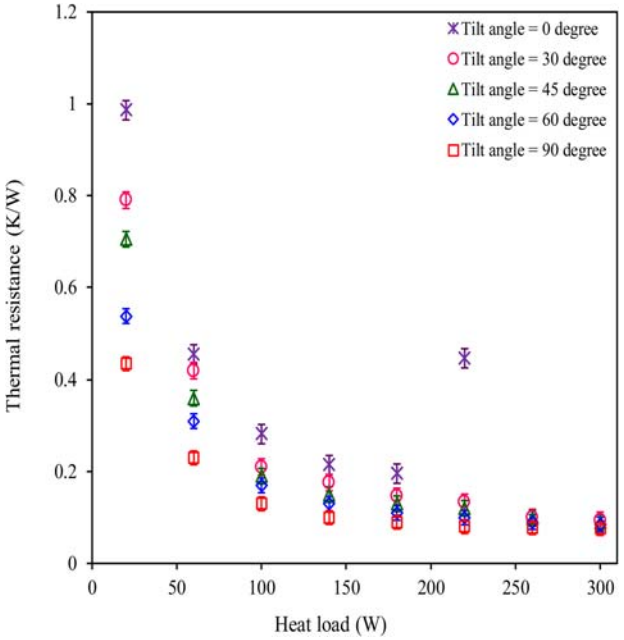

Fig. 11 Thermal resistance versus heat load (different tilt angles)

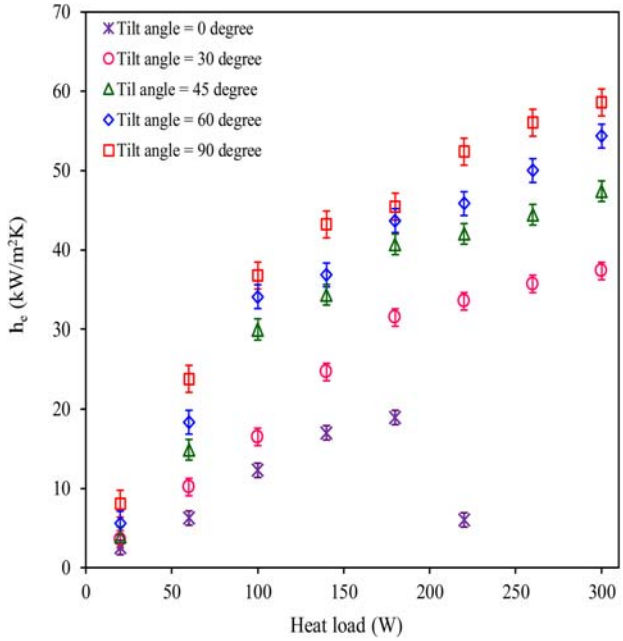

Fig. 12 Evaporator heat transfer coefficient versus heat load (different tilt angles)

liquid flow occurs fast from the condenser to the evaporator to occupy the space of vaporized liquid. The flow of liquid is comparatively slow at lower inclinations, and it slows down the heat transfer process. For the horizontal orientation (0 deg), the mini-loop thermosyphon stops working after 180 W, which is observed with a sudden increase in the thermal resistance, and it is due to the dry out phenomenon occurring at the evaporator. The liquid flow from the condenser is slow at this inclination because the liquid is fully distributed in the liquid line, and the effect of gravity is less in the horizontal orientation. But as inclination increases, the liquid flows fast to the evaporator to prevent dry out leading to the normal working of the mini-loop thermosyphon with lower thermal resistances at higher heat inputs.

The thermal resistance varies from 0.99 K/W to 0.44 K/W for different inclinations at the lowest applied heat load of 20 W, and it represents a decrease of 55% for 90 deg inclination compared with the horizontal orientation. This variation decreases with an increase in the heat load, and at the highest applied heat load of 300 W, the maximum variation is 0.018 K/W for inclinations ranging from 30 deg to 90 deg. The best performance of the mini-loop thermosyphon is observed in the vertical orientation (90 deg) with the lowest thermal resistances at all heat loads. This confirms the influence of inclination on the thermal performance of mini-loop thermosyphon.

Figure 12 shows the influence of the tilt angle and heat load on the evaporator heat transfer coefficient of the mini-loop thermosyphon for the optimum filling ratio. It can be seen that the evaporator heat transfer coefficient increases with enhancements in the heat load and tilt angle. The vaporization rate is increased with heat load for all tilt angles to get higher evaporator heat transfer coefficients. When the tilt angle is increased, the liquid easily flows to the evaporator from the condenser, and vapor flow becomes smoother at higher tilt angles. In all inclinations, a sufficient quantity of liquid is available for the normal working of the mini-loop thermosyphon. It shows that the effect of gravity plays a key part in increasing the evaporator heat transfer coefficient in vertical inclination.

The capillary action of the microfins works in all tilt angles to speed up the rewetting process. Since the heater is present only in the evaporator region, the boiling rate will be high in this region even though the heat loss to the reservoir is unavoidable. This heat loss to the reservoir acts like preheating and helps to reduce the boiling time at the evaporator. The optimum filling ratio also ensures a sufficient quantity of liquid at all tilt angles. The variation of the evaporator heat transfer coefficient increases with heat input and tilt angles, and it is due to the changes in liquid supply to the evaporator, vaporization rate, heat load, and properties of water. The distribution of the heat pipe fluid on the evaporator surface inside the liquid line and vapor line greatly affects the values of heat transfer coefficient in all orientations. A sudden decrease in the evaporator heat transfer coefficient is observed for the horizontal orientation after 180 W, and it is due to the partial dry out at the evaporator with insufficient liquid supply. The heat transfer coefficient at the evaporator varies in the span of 2.54–58.59 kW/m^2 K for the applied heat loads and tilt angles.

Figure 13 is the representation of the variation of the average condenser heat transfer coefficient with heat load and tilt angle at the optimum filling ratio. The condensation process is directly connected with the vaporization process at the evaporator. The condenser length is found to be sufficient for condensing all the vapors reaching the evaporator even at higher heat inputs of 300 W. The rate of heat rejection at the condenser depends mainly on the vaporization rate at the evaporator as the mini-loop thermosyphon is fully insulated with thick glass wool. The latent heat absorbed during vaporization is rejected at the condenser to the cooling water. In the condenser, the condensation starts when vapors reach the condenser inlet, and this process continues until all vapors are condensed. Sub cooling of the liquid is also present at lower heat loads, and it reduces with enhancement in heat load as the full length of the condenser is utilized for the condensation process.

At higher heat loads, the increase in vapor formation improves the mass flow rate of vapor as the vapors experience a pushing effect from the newly generated vapors. The mass flow rate of vapor, coolant specifications, condenser dimensions, and surface properties are the major factors affecting the condensation phenomenon. The cooling water flow rate and temperature are found to be sufficient for the condensation of vapors even at high heat loads of 300 W. Since the evaporator heat transfer coefficient value is high at higher heat inputs and tilt angles, the same trend is observed for the condenser heat transfer coefficient. A sharp decrease in the condenser heat transfer coefficient is observed above 180 W for the horizontal orientation, and it represents the decrease in

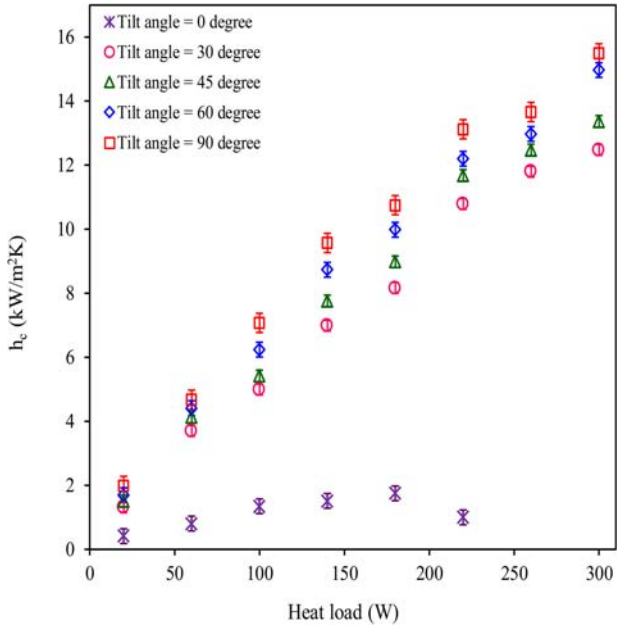

Fig. 13 Condenser heat transfer coefficient versus heat load (different tilt angles)

condensation. The condenser heat transfer coefficient values range from 0.41 kW/m^2 K to 15.49 kW/m^2 K for different heat inputs and tilt angles.

Figure 14 indicates the changes in the evaporator surface temperature with an increase in the heat load and tilt angle for the filling ratio of 30%. It shows that the evaporator surface temperature decreases with an increase in the tilt angle and increases with an increase in the heat input. The evaporator wall temperature is influenced by the vaporization at the evaporator as higher vaporization rate removes more heat from the evaporator surface to give a lower evaporator wall temperature. The increase in evaporator temperature with an increase in the heat input shows that the increase in vapor generation rate is less compared with the heat transfer rate from the heater to the evaporator surface. When the mini-loop thermosyphon reaches steady-state at any heat load, the evaporator temperature remains the same, and it represents a constant rate of heat transfer from the evaporator to the condenser. At higher tilt angles, the flow rate of the liquid increases to the evaporator, and the incoming liquid to reservoir absorbs heat before the vaporization process in the evaporator. This increased flow rate increases the convective boiling in the evaporator-reservoir region to give a lower evaporator wall temperature. In the horizontal orientation, the flow of liquid is not fully assisted by gravity that decreases the flow rate of liquid and increases the evaporator wall temperature. The sudden increase in the evaporator wall temperature at 220 W shows that the liquid reaching the evaporator is not sufficient to prevent the temperature increase at the evaporator. The temperature of the evaporator surface lies in the range of 34.6–68.6 °C for the vertical orientation of the heat pipe.

Figure 15 shows the change of effective thermal conductivity of mini-loop thermosyphon for various heat loads and tilt angles at the optimum filling ratio of 30%. Effective thermal conductivity indicates how quickly the heat can be transferred from the evaporator to the condenser, and it can be observed that K_{eff} enhances with heat input and tilt angle. The increase in heat transfer at high heat loads and corresponding lower thermal resistance values give high values for the effective thermal conductivity at higher heat loads. The highest effective thermal conductivity values are obtained for the vertical orientation of the mini-loop thermosyphon for all heat loads. The effective thermal conductivities lie in the range of 2.43–31.5 kW/m K for all heat loads and tilt angles. A highest value of 31.5 kW/m K is obtained for the effective thermal conductivity with a tilt angle of 90 deg at the peak heat load of 300 W. A decrease of effective thermal conductivity is observed at 220 W for the horizontal orientation because mini-loop thermosyphon experienced a partial dry out.

Figure 16 shows the variation of thermal efficiency with an increase in heat inputs and tilt angles at the optimum filling ratio of 30%. It is observed that the thermal efficiency has an increasing trend with an increase in heat load and tilt angle. Similarly, the value of thermal efficiency is always below 100%. This indicates that all the heat applied at the evaporator is not transferred to the condenser in the form of vapor flow. However, at higher heat loads, more heat is utilized for the vapor generation, and more heat is transferred to

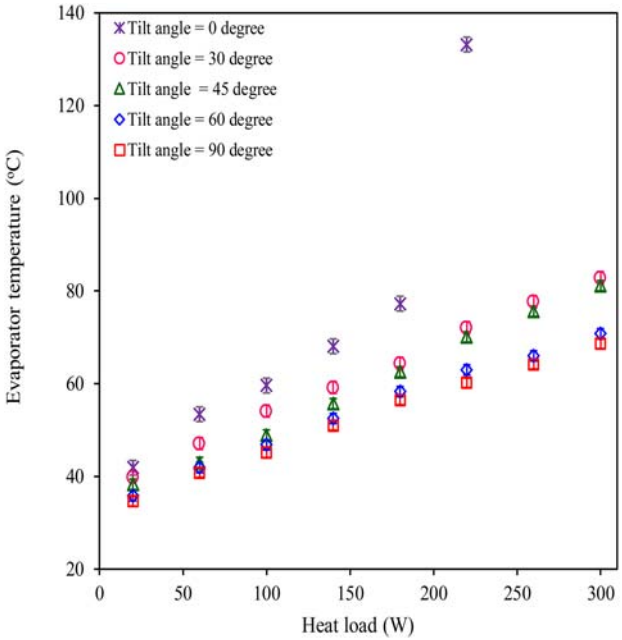

Fig. 14 Evaporator wall temperature versus heat load (different tilt angles)

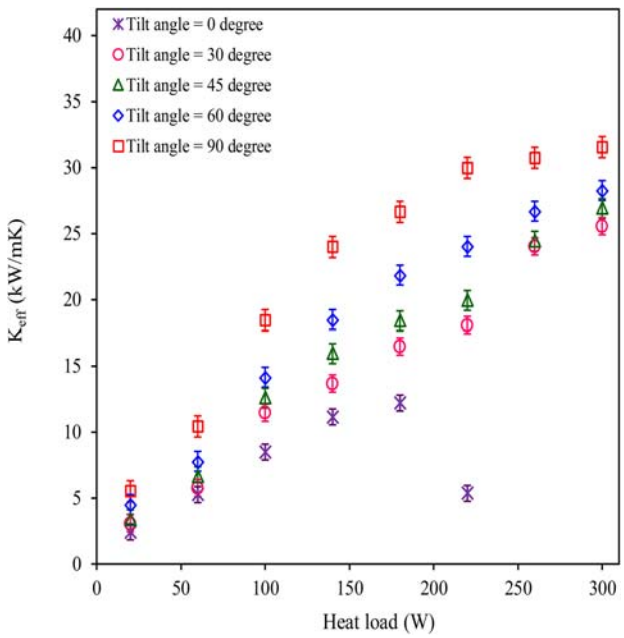

Fig. 15 Effective thermal conductivity versus heat load (different tilt angles)

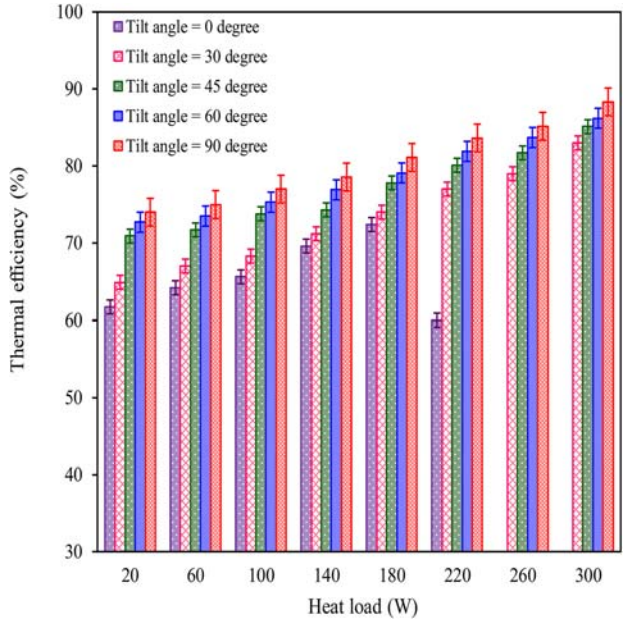

Fig. 16 Thermal efficiency versus heat load (different tilt angles)

the condenser which gives higher thermal efficiency values. Similarly, as tilt angle increases, the increased flow of liquid to evaporator absorbs more heat from the heater and delivers at the condenser side to have higher thermal efficiency values. The thermal efficiency values lie in the range of 61.7–88.3% for all tilt angles and heat inputs. The highest thermal efficiency is observed at 300 W for 90 deg tilt angle with the optimum filling ratio of 30%.

The decrease in thermal efficiency for the horizontal orientation is due to the slow supply of working fluid to the evaporator which delays the vaporization and increases the heat loss to other parts of the heat pipe. It can be seen that heat loss is present in all inclinations and tilt angles, and it is reduced to a minimum value at 90 deg tilt angle and higher heat loads. Since the material of mini-loop thermosyphon is copper and the thermal conductivity value of copper is high, there are more chances of heat loss to the reservoir and liquid line. But a maximum thermal efficiency is achieved by optimizing FR, using vertical tilt angle and higher heat inputs.

These results indicate that both FR and tilt angles are the two major factors influencing the heat transfer performance of the mini-loop thermosyphon. The optimum filling ratio for this mini-loop thermosyphon is 30% of the total volume. Similarly, the best heat transfer performance is obtained with the tilt angle of 90 deg.

4 Conclusion

An experimental heat transfer study was conducted on a mini-loop thermosyphon with the use of distilled water as the heat pipe fluid at various filling ratios and tilt angles. The experimental results showed the presence of an optimum filling ratio for this mini-loop thermosyphon, and it is 30% of the total volume. A lowermost heat pipe resistance value of 0.076 K/W and uppermost evaporator heat transfer coefficient value of 58.6 kW/m^2 K were observed with the 30% FR at 300 W. Similarly, the evaporator wall temperature showed an average reduction of 9.2 °C, and thermal efficiency showed an average enhancement of 12.2% at optimum FR compared with 70% FR. The tilt angle also influenced the heat transfer performance, and the best performance is observed with the 90 deg tilt angle at the optimum FR. The evaporator and condenser heat transfer coefficient values were in the ranges of 2.54–58.59 kW/m^2 K and 0.41–15.49 kW/m^2 K, respectively, for different tilt angles and heat loads. Similarly, effective thermal conductivity and thermal efficiency were in the ranges of 2.43–31.5 kW/m K and 61.7–88.3% for all tilt angles and heat inputs, respectively. The evaporator wall temperature was in the range of 34.6–68.6 °C for different heat loads in the vertical orientation of the heat pipe. Similarly, a comparison of the plain and microfinned evaporator of mini-loop thermosyphon showed the influence of microfins in the improvement of heat transfer. These results show that the mini-loop thermosyphon is a possible solution for electronics cooling, and its best performance is obtained when the optimum FR and vertical orientation are employed. Heat transfer performance of the mini-loop thermosyphon can be improved by coating nanoparticles at various thicknesses on the inner surfaces of the evaporator and the loop.

Acknowledgment

Authors appreciate the Karunya Institute of Technology and Sciences for extending all infrastructure facilities needed for this study. They also express their gratitude to Mr. R. Jaya Seelan and Mr. C. John Kennedy of the Karunya Institute of Technology and Sciences for all their help during fabrication and testing of mini-loop thermosyphon.

Funding Data

- Department of Science and Technology (DST), Science and Engineering Research Board (SERB), (SB/FTP/ETA-362/2012), New Delhi, India

Nomenclature

c = specific heat of cooling water (J/kg K)
h = heat transfer coefficient (W/m^2 K)
m = mass flow rate of cooling water (kg/s)
q = heat flux (W/m^2)
A = area of heat transfer (m^2)
I = current (A)
L = span of mini-loop thermosyphon from the evaporator to the condenser (m)
T = temperature (°C)
V = voltage (V)
Q_a = applied heat input (W)
Q_c = heat removed at condenser (W)
R_t = heat pipe thermal resistance (K/W)
FR = filling ratio (%)
ID = inner diameter (m)
LPH = liters per hour
OD = outer diameter (m)

Greek Symbols

η_t = thermal efficiency of heat pipe (%)
Δ = change

Subscripts

c = condenser
c/s = cross-sectional
e = evaporator
ec = between the evaporator and condenser
vc = vapor at the condenser
ve = vapor at the evaporator
vs = between vapor and surface
w = water

References

[1] Tharayil, T., Asirvatham, L. G., Cassie, C. F. M., and Wongwises, S., 2017, "Performance of Cylindrical and Flattened Heat Pipes at Various Inclinations Including Repeatability in Anti-Gravity—A Comparative Study," Appl. Therm. Eng., **122**, pp. 685–696.
[2] Tharayil, T., Asirvatham, L. G., Dau, M. J., and Wongwises, S., 2017, "Entropy Generation Analysis of a Miniature Loop Heat Pipe With Graphene-Water

Nanofluid: Thermodynamics Model and Experimental Study," Int. J. Heat Mass Transf., **106**, pp. 407–421.
[3] Na, M. K., Jeon, J. S., Kwak, H. Y., and Nam, S. S., 2001, "Experimental Study on Closed-Loop Two-Phase Thermosyphon Devices for Cooling MCMs," Heat Transf. Eng., **22**(2), pp. 29–39.
[4] Gima, S., Nagata, T., Zhang, X., and Fujii, M., 2005, "Experimental Study on CPU Cooling System of Closed-Loop Two-Phase Thermosyphon," Heat Transf.—Asian Res., **34**(3), pp. 147–159.
[5] Sarno, C., Tantolin, C., Hodot, R., Maydanik, Y., and Vershinin, S., 2013, "Loop Thermosyphon Thermal Management of the Avionics of an In-Flight Entertainment System," Appl. Therm. Eng., **51**(1–2), pp. 764–769.
[6] Khrustalev, D., 2002, "Loop Thermosyphons for Cooling of Electronics," 18th IEEE SEMI-THERM Symposium, San Jose, CA, Mar. 12–14, IEEE, New York, pp. 145–150.
[7] Chang, C. C., Kuo, S. C., Ke, M. T., and Chen, S. L., 2010, "Two-Phase Closed-Loop Thermosyphon for Electronic Cooling," Exp. Heat Transf., **23**(2), pp. 144–156.
[8] Chehade, A. A., Gualous, H. L., Masson, S. L., Victor, I., and Damaj, N. A., 2014, "Experimental Investigation of Thermosyphon Loop Thermal Performance," Energy Convers. Manage., **84**, pp. 671–680.
[9] Franco, A., and Filippeschi, S., 2012, "Experimental Analysis of Closed Loop Two Phase Thermosyphon (CLTPT) for Energy Systems," Microgravity Sci. Technol., **24**, pp. 165–179.
[10] Zhang, P., Wang, B., Shi, W., and Li, X., 2015, "Experimental Investigation on Two-Phase Thermosyphon Loop With Partially Liquid-Filled Downcomer," Appl. Energy, **160**, pp. 10–17.
[11] Gualous, H. L., Masson, S. L., and Chahed, A., 2017, "An Experimental Study of Evaporation and Condensation Heat Transfer Coefficients for Looped Thermosyphon," Appl. Therm. Eng., **110**, pp. 931–940.
[12] Godson, L., Raja, B., Lal, D. M., and Wongwises, S., 2010, "Enhancement of Heat Transfer Using Nanofluids-An Overview," Renew. Sustain. Energy Rev., **14**(2), pp. 629–641.
[13] Asirvatham, L. G., Nimmagadda, R., and Wongwises, S., 2013, "Heat Transfer Performance of Screen Mesh Wick Heat Pipes Using Silver-Water Nanofluid," Int. J. Heat Mass Transf., **60**, pp. 201–209.
[14] Kumaresan, G., Venkatachalapathy, S., Asirvatham, L. G., and Wongwises, S., 2014, "Comparative Study on Heat Transfer Characteristics of Sintered and Mesh Wick Heat Pipes Using CuO Nanofluids," Int. Commun. Heat Mass Transf., **57**, pp. 208–215.
[15] Asirvatham, L. G., Nimmagadda, R., and Wongwises, S., 2013, "Operational Limitations of Heat Pipes With Silver-Water Nanofluids," ASME J. Heat Transf., **135**(11), p. 111011.
[16] Tharayil, T., Asirvatham, L. G., Rajesh, S., and Wongwises, S., 2017, "Effect of Nanoparticle Coating on the Performance of a Miniature Loop Heat Pipe for Electronics Cooling Applications," ASME J. Heat Transf., **140**(2), p. 022401.
[17] Ninolin, E., Lazarus, G. A., and Ramachandran, K., 2016, "Thermal Performance of a Compact Loop Heat Pipe With Silver-Water Nanofluid," Appl. Mech. Mater., **852**, pp. 666–674.
[18] Asirvatham, L. G., Raja, B., Lal, D. M., and Wongwises, S., 2011, "Convective Heat Transfer of Nanofluids With Correlations," Particuology, **9**(6), pp. 626–631.
[19] Solomon, A. B., Roshan, R., Vincent, W., Karthikeyan, V. K., and Asirvatham, L. G., 2015, "Heat Transfer Performance of an Anodized Two-Phase Closed Thermosyphon With Refrigerant as Working Fluid," Int. J. Heat Mass Transf., **82**, pp. 521–529.
[20] Asirvatham, L. G., Wongwises, S., and Babu, J., 2015, "Heat Transfer Performance of a Glass Thermosyphon Using Graphene-Acetone Nanofluid," ASME J. Heat Transf., **137**(11), p. 111502.
[21] Kumaresan, G., Venkatachalapathy, S., and Asirvatham, L. G., 2014, "Experimental Investigation on Enhancement in Thermal Characteristics of Sintered Wick Heat Pipe Using CuO Nanofluids," Int. J. Heat Mass Transf., **72**, pp. 507–516.
[22] Ramachandran, R., Ganesan, K., Rajkumar, M. R., Asirvatham, L. G., and Wongwises, S., 2016, "Comparative Study of the Effect of Hybrid Nanoparticle on the Thermal Performance of Cylindrical Screen Mesh Heat Pipe," Int. Commun. Heat Mass Transf., **76**, pp. 294–300.
[23] Solomon, A. B., Ramachandran, K., Asirvatham, L. G., and Pillai, B. C., 2014, "Numerical Analysis of a Screen Mesh Wick Heat Pipe With Cu/Water Nanofluid," Int. J. Heat Mass Transf., **75**, pp. 523–533.
[24] Tharayil, T., Asirvatham, L. G., Ravindran, V., and Wongwises, S., 2016, "Effect of Filling Ratio on the Performance of a Novel Miniature Loop Heat Pipe Having Different Diameter Transport Lines," Appl. Therm. Eng., **106**, pp. 588–600.
[25] Tharayil, T., Asirvatham, L. G., Ravindran, V., and Wongwises, S., 2016, "Thermal Performance of Miniature Loop Heat Pipe With Graphene-Water Nanofluid," Int. J. Heat Mass Transf., **93**, pp. 957–968.
[26] Agostini, F., Habert, M., Molitor, F., Flüeckiger, R., Kaufmann, L., Bergamini, A., Rossi, M., and Besana, S., 2014, "Double-Loop Thermosyphon for Electric Components Cooling," IEEE Trans. Compon. Packag. Technol., **4**(2), pp. 223–231.
[27] Khodabandeh, R., 2004, "Thermal Performance of a Closed Advanced Two-Phase Thermosyphon Loop for Cooling of Radio Base Stations at Different Operating Conditions," Appl. Therm. Eng., **24**(17–18), pp. 2643–2655.
[28] Chehade, A., Gualous, H. L., Masson, S. L., and Lepinasse, E., 2015, "Experimental Investigations and Modeling of a Loop Thermosyphon for Cooling With Zero Electrical Consumption," Appl. Therm. Eng., **87**, pp. 559–573.
[29] Mameli, M., Mangini, D., Vanoli, G. F. T., Araneo, L., Filippeschi, S., and Marengo, M., 2016, "Advanced Multi-Evaporator Loop Thermosyphon," Energy, **112**, pp. 562–573.
[30] He, H., Furusato, K., Yamada, M., Shen, B., Hidaka, S., Kohno, M., Takahashi, K., and Takata, Y., 2017, "Efficiency Enhancement of a Loop Thermosyphon on a Mixed-Wettability Evaporator Surface," Appl. Therm. Eng., **123**, pp. 1245–1254.
[31] Tharayil, T., Asirvatham, L. G., Rajesh, S., and Wongwises, S., 2018, "Thermal Management of Electronic Devices Using Combined Effects of Nanoparticle Coating and Graphene–Water Nanofluid in a Miniature Loop Heat Pipe," IEEE Trans. Compon. Packag. Technol., **8**(7), pp. 1241–1253.